JLU
NEUE WEGE. SEIT 1607.

JUSTUS-LIEBIG-
UNIVERSITÄT
GIESSEN

Bachelorarbeit

Development of a deep neural network-based pulse shape discrimination for organic scintillators using GEANT4 generated pulses

Frederik Vincent Uhlemann

Sommersemester 2024

Bachelorarbeit

Development of a deep neural network-based pulse shape discrimination for organic scintillators using GEANT4 generated pulses

zur Erlangung des akademischen Grades
Bachelor of Science (B. Sc.)

an der

Justus - Liebig - Universität Gießen
II. Physikalisches Institut

Sommersemester 2024

vorgelegt von :	Frederik Vincent Uhlemann
am :	08.09.2024
Studiengang :	Physik
Erstgutachter :	Prof. Dr. Christoph Scheidenberger
Zweitgutachter :	Dr. Jens Sören Lange

Abstract

Since nuclear fission is a very complex and not fully understood physical process, it is an interesting field for theoretical and experimental investigation. This study analyses the method of pulse shape discrimination for a measurement related to nuclear fission.
Organic scintillators are often used to measure prompt neutrons and gammas from nuclear fission. It is investigated how the neutrons and gammas can be distinguished from their different pulse shapes. A deep neural network is used for this purpose. This network is trained with pulse shapes generated by Geant4 and later tested with experimental data.
This work shows that simulated Geant4 data can be successfully used to train a deep neural network that is able to distinguish experimental pulse shapes. This offers a promising approach for future measurements in nuclear fission studies.

Acknowledgment

I would like to extend my gratitude to Heinrich Wilsenach for introducing me to the subject of nuclear astrophysics and Geant4, and for explaining every question to me in the finest detail. Special thanks to Annesha Karmakar for her help with neural networks. I would also like to thank all members of the IONAS group for introducing me to scientific work and giving me valuable feedback. I have learnt a lot in my two years with all of you.

Contents

List of abbreviations **11**

1. Introduction **13**

2. Physics concepts **14**
2.1. Interaction of neutral particles in matter 14
2.1.1. Gammas 14
2.1.2. Neutrons 15
2.2. Scintillators and PMT's 16
2.2.1. Scintillators 16
2.2.2. Photo multiplier tube 17
2.3. Deep neural networks 19
2.3.1. L_2 regularization 19
2.3.2. Confusion matrix 19
2.3.3. Receiver operating characteristic (ROC) 21

3. Monte-Carlo simulation of scintillators with GEANT4 **22**
3.1. Introduction to GEANT4 22
3.2. Simulation setup 22
3.2.1. Geometry 23
3.2.2. Properties of used scintillators 24
3.2.3. Simulated particles and yields 27
3.2.4. Example runs 28
3.3. Simulation of electronic effects 29

4. Pulse Shape Analysis **34**
4.1. Results from Simulation 34
4.2. Charge integration method 35
4.2.1. EJ301 36
4.2.2. EJ276 37
4.3. Deep neural network 38
4.3.1. Structure of DNN 38
4.3.2. Feature analysis 40

4.3.3. Testing the DNN 41

5. Results and discussion **46**
5.1. Comparison of ROC-curves 46
5.2. Comparison between CI and DNN methods 46
5.2.1. plastic scintillator- EJ276 46
5.2.2. Experimental data 48
5.3. Investigation of different Slab lengths 49

6. Conclusion and outlook **53**

List of Figures **54**

List of Tables **56**

Bibliography **57**

A. Single Pulses **60**

B. Calibration **62**

List of abbreviations

JLU ..... Justus - Liebig - Universität

PSD ..... Pulse shape discrimination

PMT ..... Photomultiplier tube

CI ..... Charge integration

CFD ..... Constant fraction discriminator

DNN ..... Deep neural network

CNN ..... Convolutional neural network

ROC ..... Receiver operating characteristic

ADC ..... Analogue to digital converter

MC ..... Monte-Carlo

FWHM ..... Full Width at Half Maximum

QE ..... Quantum Efficiency

TTS ..... Transit time spread

1. Introduction

Nuclear fission is a phenomenon that has been studied for a long time, it was first discovered in 1938 by Hahn and Strassman [1]. They observed significantly lighter particles than uranium, in the irradiation of uranium with neutrons. Back then, this phenomenon was investigated further, but quickly became interesting for technical research, like nuclear power generation.
The process of nuclear fission is also very interesting for nuclear astrophysics, as it plays a role in the formation of heavy elements in the universe [2]. Since the fission process is very complicated, as many particles are involved, it is not yet fully understood from a theoretical point of view. Schunk [3] describes the current research situation for theoretical models of nuclear fission. The technical development of recent years has made it possible to improve the experimental investigation of this process, a comprehensive overview can be found in [4].
Currently there is little experimental data on prompt neutrons and prompt gammas that are produced during nuclear fission. These are difficult to measure, but are important for understanding nuclear fission. This work is a small study in the context of a larger investigation, for a design of a device that should be able to measure the prompt neutrons and gammas, located at the FRS Ion Catcher. A first interesting measurement would be the neutron multiplicities as a function of the fission fragment mass.
The neutrons and gammas in the planned experiment will be measured with organic scintillators, and can be distinguished using the method of pulse shape discrimination (PSD). Due to the different interaction of the particles in the material, results in slightly different pulse shapes, this effect can be used to differentiate between neutrons and gammas.
Chapter 2 of this thesis gives a brief introduction to the basic physics and technical concepts used in this work. The pulse shapes of prompt neutron and gammas from ^{252}Cf spontaneous fission events in organic scintillators are simulated in Chapter 3 using Geant4. After that a deep neural network (DNN) is trained with the obtained simulation data to distinguish between neutrons and gammas. In addition, the network is tested with experimental data and the effect of different scintillator geometries on the pulse shape discrimination capability is investigated.

2. Physics concepts

This chapter explains some basic physical concepts for the interaction of neutrons and gammas in materials and their detection by scintillators. Additional deep neural networks and important metrics for classification problems are discussed.

2.1. Interaction of neutral particles in matter

As mentioned at the beginning, neutrons and gammas are the particles that are measured and analysed. Therefore, the interaction of these particles with matter will be briefly explained. A very detailed introduction to the subject is given by Knoll [5] and Leo [6].

2.1.1. Gammas

When gamma rays interact with matter, they can be absorbed, a process that can be described macroscopically by exponential behaviour:

$$I(d) = I_0 \cdot e^{-\mu d} \tag{2.1}$$

Where the intensity (I) decreases exponentially with the thickness d from an initial intensity I_0, this depends on a material constant μ, the linear attenuation coefficient. At the microscopic level, gammas can interact with matter in three different ways:

Photoelectric effect The mechanism of the photoelectric effect is that a gamma gives energy to a bound electron of an atom, this electron is then released from the atom. The energy of the photon must be greater than the binding energy E_B of this electron, the electron receives the photon energy ($h\nu$) minus its binding energy:

$$E = h\nu - E_B \tag{2.2}$$

This interaction is dominating for low energy photons ($< 100\,\mathrm{keV}$).

Compton Scattering For Compton scattering the incident gamma again interacts with a charged particle, mostly an electron. This recoil electron gets some of the incident gamma energy, the gamma changes its direction. The conservation of energy and momentum leads to the equation:

$$h\nu' = \frac{h\nu}{1 + \frac{h\nu}{m_0 c^2}(1 - \cos\theta)} \tag{2.3}$$

Where $h\nu$ is the energy of the incident photon and $h\nu'$ the energy of the scattered photon, the scatter angle isθ and the rest mass of the recoil m_0.

This process is often repeated within a material. It is the dominating interaction for medium energy photons ($\approx 100\,\text{keV} - 10\,\text{MeV}$).

Pair production In the process of pair production, a matter-antimatter pair is produced inside the Coulomb field of an atom. For this to happen, the photon must exceed a certain energy, for the most common pair, the electron-positron pair, it is the rest mass of these two particles:

$$E_\gamma \leq 2m_e c^2 \tag{2.4}$$

Where m_e is the mass of the electron/positron and c the light speed, to get from a mass to an energy. That means the gamma needs at least the energy of 1022 keV to produce a pair. This process dominates in the higher energy regions ($\leq 10\,\text{MeV}$)

2.1.2. Neutrons

Neutrons also carry no charge, which means they cannot interact with the material through the Coulomb force. In fact, they can only interact with the atomic nucleus, and because they are very small compared to the atomic shell, neutrons can travel long distances, up to a few centimetres, without interacting with a material. In general, two different interactions can appear for a neutron in a material: scattering or absorption. As with the gammas, the interaction is discussed for different energy ranges.

Slow Neutrons Slow neutrons have low kinetic energy or speed. Because of this small energy, they can transfer this energy to a single nucleus through elastic scattering. This interaction is common in materials, but cannot be used for detection.
Another interaction is the neutron capture, where a neutron is captured

from a nucleus. This nucleus is then in an excited state and will usually emit gammas to reach a stable state. The highest cross sections for capture reactions have neutrons in a thermal energy range, which is equal to $\approx 0.025\,\text{eV}$. It is often the case that a slow neutron is brought to such a low energy range by elastic scattering and then absorbed.

Fast Neutrons For fast neutrons, inelastic scattering becomes dominant. So the neutron scatters with a nucleus. This is then called a **recoil nucleus**, the neutron is not stopped but changes its kinetic energy and momentum. Through the conversation of momentum and energy in a scattering process, the neutron can transfer more of its energy to light nuclei. This is the reason why neutron detectors are made of organic materials, because they contain a lot of hydrogen atoms. And a neutron can give all of its energy to a single hydrogen atom.
If the kinetic energy is very high, the neutron scatters many times by elastic scattering inside the material.

2.2. Scintillators and PMT's

2.2.1. Scintillators

In general, a scintillator is a detector material that produces optical photons when a particle interacts with it. The physical process of this behaviour is known as **luminescence**. The incident particles cause atoms or molecules of the scintillator material, to be in an excited state. When these states are de-exited, optical photons are emitted.
There are two groups of scintillators, inorganic and organic ones. This study concentrates on organic scintillators, because they are better at detecting neutrons, as explained in the chapter 2.1.2.
Organic scintillators consist of organic molecules, so it does not matter in what aggregate state the organic material is in. For this reason, organic scintillators can be liquid or plastic. The functionality is based on the so-called π electron structure, which is a combination of carbon and hydrogen orbitals. The basic functionality is shown in Figure 2.1, the singlet spin states decay after a short time through fluorescence. The triplet states are more stable and take longer to decay with phosphorescence. These two effects produce optical photons with two different decay time components. A fast time component for **fluorescence** and a slow one for **phosphorescence**. This is the basic principle for producing different pulse shapes within an organic scintillator

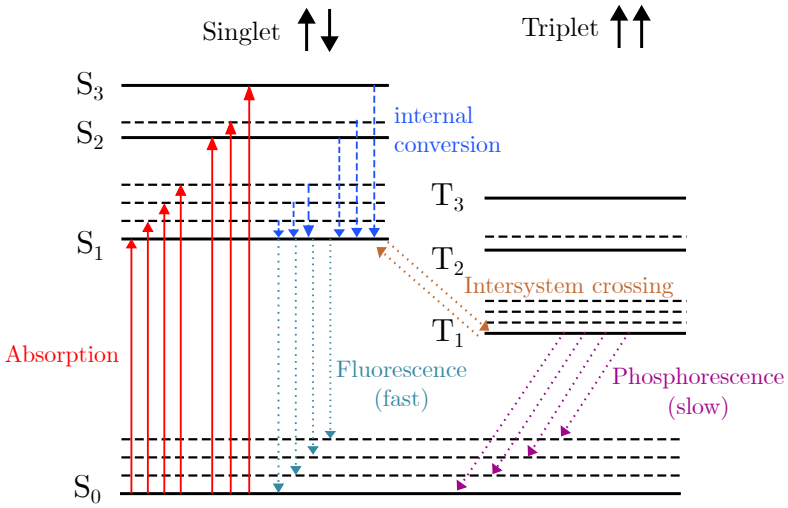

Figure 2.1.: Energy Levels for an organic structure, with an π-orbital. There are Singlet states with Spin zero and Triplet ones with Spin 1. This graphic is based on [7]

The decay can be described with falling exponential functions, for the two different decay times:

$$f(t) = A_1 \mathrm{e}^{-\frac{t}{\tau_1}} + A_2 \mathrm{e}^{-\frac{t}{\tau_2}} \tag{2.5}$$

Were τ are the time constants and A their impact on the total pulse shape f.

2.2.2. Photo multiplier tube

A scintillator alone can not be used for measuring the neutral particles, because it only produces 100 to 1000 optical photons. This photon are converted with another device, the photomultiplier tube, into a measurable electronic signal. The basic principle is described in Figure 2.2. The multiplication of electrons inside a PMT depends on the number of dynodes, and more dynodes mean a higher multiplication. Generally the gain is between 10×10^6-10×10^7.
Besides the gain of a PMT, the **transit time spread** (TTS) is an important

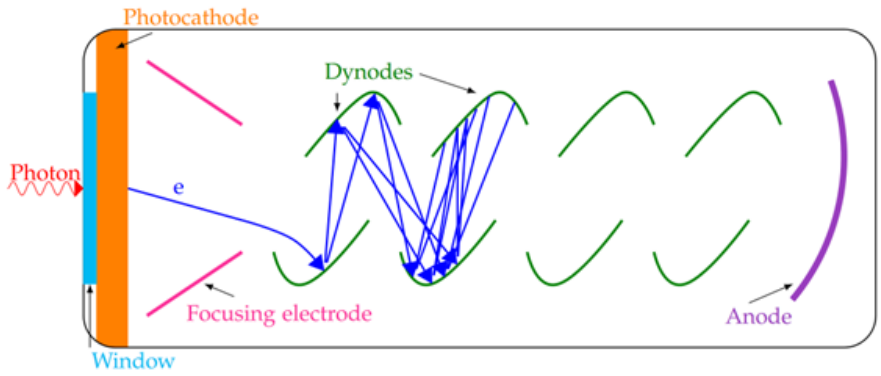

Figure 2.2.: Basic schematics of a photomultiplier tube. The photoelectric effect converts an optical photon into an electron at the photocathode. This single electron then hits a dynode. This causes electrons to be knocked out of it. This leads to an avalanche of electrons, which can be measured as a current at the anode. The figure is from [8]

characteristic. The produced electrons of one single photon have a spread in their time on the anode. The reason is that the electrons travel slightly different paths inside the PMT. The result is shown in **??**. The FWHM of this spread is called the TTS and is an important characteristic of PMTs.

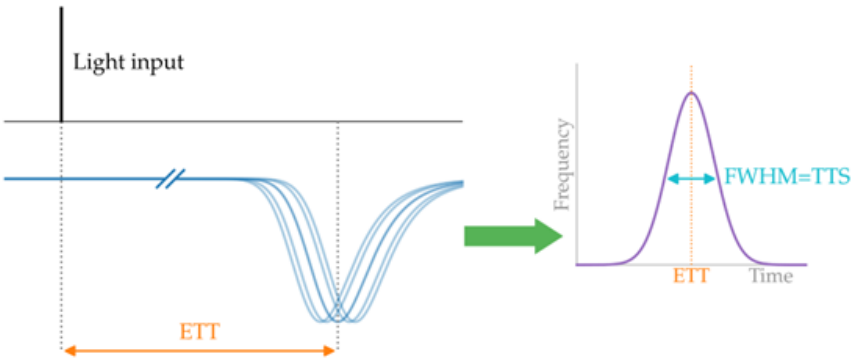

Figure 2.3.: Transit time spread inside a PMT, shown for a single photon event, the slightly different paths of the electrons are shifted to each other. The end result is a distribution with one FWHM, which is the TTS. The figure is again from [8]

2.3. Deep neural networks

A deep neural network is a specification of an artificial neural network. This topic is very complex, and a lot of literature can be found, a good overview is given by Géron in his book [9]. In the following, the most important concepts will be shortly discussed.
The most important key concept of a neural network is a single artificial neuron, in principle, it is based on a biological neuron. It activates its output at a certain state of its inputs. The activation function can take different forms, as example, step-, logistic-, and hyperbolic tangent functions are used.
A single neuron is not really powerful, but when multiple of them are connected together, a network is created that can be surprisingly complex. Typically, these neurons are arranged in layers, which are one-dimensional vectors of the neurons. Then a neural network consists of an input layer, an output layer and often hidden layers in between.
The speciality of a deep neural network is that all neurons are fully connected to each other, this means that very complex logical processes can occur within such a network. In this work, the DNN is used for a binary classification problem, which means the output layer consists of only one neuron. This neuron has a sigmoid activation function, this neutron returns only two values, zero and one.
The DNN learns by trying to guess the classification of an input and at the end it compares whether it was correct, after which the weights between the neurons are adjusted. The network does this many times and continues to improve. To achieve good results in the end, many parameters have to be fine-tuned.

2.3.1. L_2 regularization

An often upcoming problem is overfitting, this means that a DNN has learnt the training data too precisely, but has no general properties to distinguish other test datasets. There are different approaches to reduce this problem, for example, regularisation.
Simply explained for L_2 regularisation, a penalty is applied to weights that are too large. The result is that all weights remain small and no specific weight becomes dominant.

2.3.2. Confusion matrix

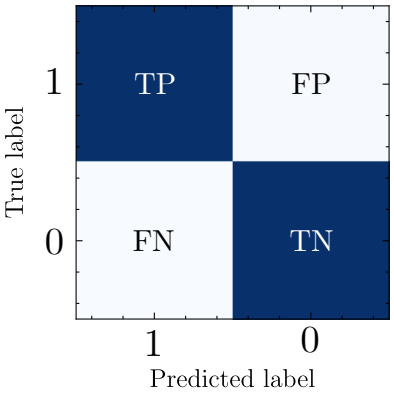

Figure 2.4.: Basic structure of a confusion Matrix for a classification problem

A typical representation of the performance of a DNN is the confusion matrix, it can be used to determine important parameters for a trained network. The matrix is the result of testing a DNN with a dataset. The basic structure for a binary problem can be seen in Figure 2.4, the classification problem of this work is a binary one since it is necessary to distinguish between two states: neutrons (1) and gammas (0).
The matrix contains the respective predicted and true values, which means the **True Positive** (TP) and **True Negativ** (TN) values. But also in addition, the **False Positive** (FP) and **False Negativ** (FN) values. These values can be used to calculate some important parameters that show the performance of a DNN.
The first value is the precision (P), this value can be calculated separately for each class, it shows how accurately that class can be determined by the DNN. It is the ratio between the correct classified values of a class to the total number of instances in these class:

$$\mathrm{P}_1 = \frac{\mathrm{TP}}{\mathrm{TP}+\mathrm{FP}} \qquad \mathrm{P}_0 = \frac{\mathrm{TN}}{\mathrm{TN}+\mathrm{FN}} \tag{2.6}$$

The recall value (R), is the ratio of correct classified instances of a class to the total number of true instances, this value represents how the classifier performs on the actual positive instances:

$$\mathrm{R}_1 = \frac{\mathrm{TP}}{\mathrm{TP}+\mathrm{FN}} \qquad \mathrm{R}_0 = \frac{\mathrm{TN}}{\mathrm{TN}+\mathrm{FP}} \tag{2.7}$$

Then the F1-score combines the precision and recall value, it is calculated with the harmonic mean between the two scores:

$$\mathrm{F1}_1 = 2\frac{\mathrm{P}_1 \times \mathrm{R}_1}{\mathrm{P}_1 + \mathrm{R}_1} \qquad \mathrm{F1}_0 = 2\frac{\mathrm{P}_0 \times \mathrm{R}_0}{\mathrm{P}_0 + \mathrm{R}_0} \tag{2.8}$$

The last value is the accuracy which combines the two different classes into one value. It measures how correct the classification is overall, but can be misleading when the datasets are not balanced. It is the ratio between all correct classified instances to all instances:

$$\mathrm{Accuracy} = \frac{\mathrm{TP}+\mathrm{TN}}{\mathrm{TP}+\mathrm{TN}+\mathrm{FP}+\mathrm{FN}} \tag{2.9}$$

2.3.3. Receiver operating characteristic (ROC)

The **Receiver operating characteristic** (ROC) curve is a commonly used method for comparing different binary classifiers. It shows the **True positive rate** (TPR) against the **False positive rate** (FPR) for one classification state. The basic principle is shown in Figure 2.5. A random classification would produce a linearly increasing line that halves the plot. A perfect classification is a rectangle shape because there are only true positive values, for most classifiers, the curve is somewhere in between. One way to compare different ROC curves is the **area under the curve** (AUC), for a perfect classification, this area would be 1.

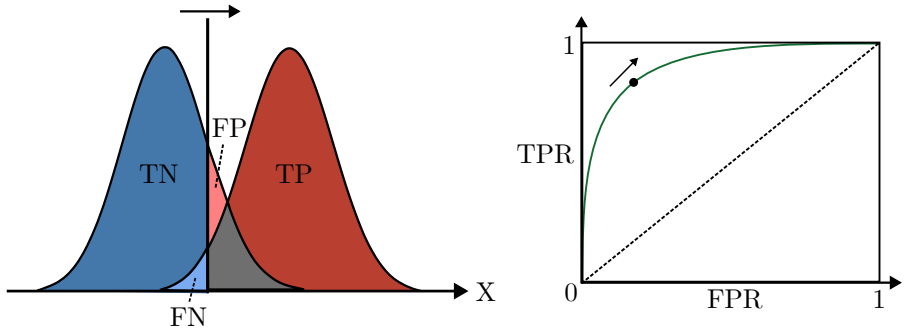

Figure 2.5.: Basic principle of a ROC curve. To generate such a curve, a variable is introduced that is independent of the actual classification. This is shown as the black vertical line in the left plot. This plot shows two overlapping distributions, the areas of which can be assigned to the four different cases of the confusion matrix. Moving the vertical line changes the areas. The resulting values can be seen in the ROC curve on the right side, which only contains the true positive and false positive rates.

3. Monte-Carlo simulation of scintillators with GEANT4

This chapter explains the Monte-Carlo simulation in Geant4, which was used to generate pulses that are later used for pulse shape discrimination. First, the simulation in Geant4 is explained, and then the further processing of the pulses in a specially programmed C++ class[1]. In the end, the generated pulses should be as similar as possible to experimentally measured pulses.

3.1. Introduction to GEANT4

Geant4 [10] is a Monte-Carlo toolkit that is written in C++. It provides several classes for simulating complex physics processes. With such a class, several objects can be created; for this physics simulation, these are, for example, particles or the trajectories of particles.
Geant4's main benefit is the simulation of the interaction of particles in materials, this simulation functions across a wide energy range and for almost all known particles. The simulation is based on the Monte-Carlo method, which mimics physical processes through the generation of parameters based on a random sampling of probability density functions.

3.2. Simulation setup

In the following, a few key classes that are important for the simulation are explained. Geant4 has the scintillation process already built in. This simulation is based on the LXe example from the Geant4 optical examples, this introduces a liquid xenon-based scintillator simulation [11].

1A class is a tool in object-orientated programming. It defines properties and usable methods for objects. In a physics context that could be the class *Lepton* that creates the object *Electron* with the attribute *mass*

3.2.1. Geometry

The geometry is defined via code sequences in the **DetectorConstruction**-class. In this simulation, the geometry is comparably easy, it consists mainly of 3 parts: The scintillator itself, an aluminium wrapping around it, and a photocathode.
Overall, two different scintillator materials are simulated, details on that can be found in the next chapter. The aluminium wrapping is needed so that the optical photons are reflected inside the scintillator, increasing the light transmission. The used reflectance as a function of energy can be seen in Figure 3.1. The reflectance of a surface indicates how much electromagnetic energy is reflected or, microscopically, how many per cent of the incoming particles are reflected. The simulated optical photons have an energy around $2 - 3\,\mathrm{eV}$, in this energy sector the reflectance is about 90%, which means there is a loss of some optical photons at the borders of the scintillator.
The photocathode absorbs the photons, and Geant4 saves every photon

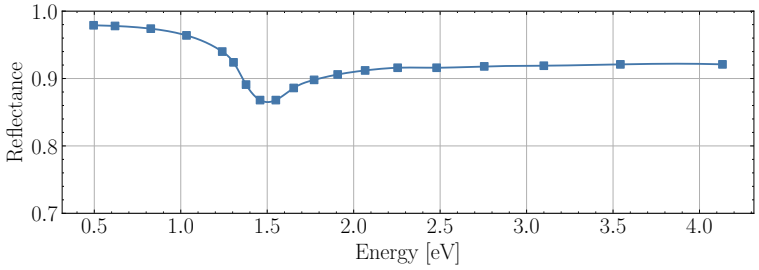

Figure 3.1.: Reflectance of aluminium in dependence of energy, it equals a wavelength range of 300 nm to 2.5 µm, this is the optical and end of the infrared region from the electromagnetic spectrum. The optical photons in this simulation have an energy range from 2.5 eV to 3.1 eV, therefore the reflectance is nearly constant slightly over 90%. The data is taken from [12]. The dip at 1.5 eV is caused by a favourable transition from the valence band to the conduction band in the aluminium.

that was absorbed and the time when this happened. The further processing of the signal is done in another class, which is explained in more detail in section 3.3.

Box geometry The first geometry is a simple cube with a size of 5 cm × 5 cm × 5 cm, it is shown in Figure 3.2. This geometry is used for the first simulations to investigate the basic pulse shapes in the organic scintillators.

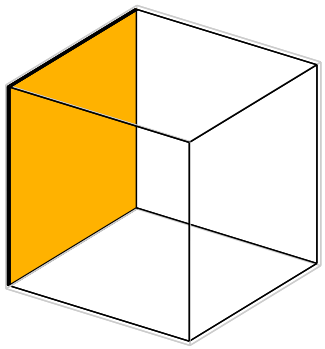

Figure 3.2.: Simple 5 cm × 5 cm × 5 cm cube, the orange area represents the photocathode of the photomultiplier tube. The aluminium wrapping can be seen in light grey.

Slab geometry The slab geometry is a more realistic shape for the upcoming experiment, as shown in Figure 3.3, it has a size of 5 cm × 5 cm × 150 cm. The question is whether the pulse shapes change significantly in such a geometry and how the capability of the pulse shape discrimination behaves. To investigate this effect the primary particles are started at different positions along the z-direction.

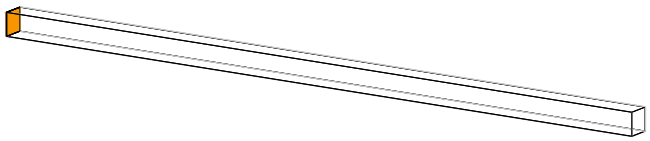

Figure 3.3.: The base area is the same as for the cube geometry, but the scintillator is now 150 cm long in the z-direction. The photocathode can be seen again in orange at one end. This could be a future geometry for the upcoming experiment, with the difference that a PMT with photocathode would be used at each end.

3.2.2. Properties of used scintillators

In order to train the network to more general data, two different organic scintillators are simulated. In Geant4 the properties of the scintillators have to be defined, the definition is separated in two steps: Definition of the material itself for the energy loss and interaction probabilities, and definition of the optical properties of the material. The following explains which properties were important in the simulation for both scintillators.

EJ301 - liquid scintillator The EJ301 liquid scintillator is based on the NE213 from **Nuclear Enterprises**, some other manufacturers have a similar one, such as the BC501 from **Saint-Gobain Crystals**. Liquid scintillators have a very good PSD compatibility and they have a relatively low flash point.
The first important characteristic is the emission spectrum, it is shown in Figure 3.4 and tells Geant4 which energies to the generated optical photons with. The second property is the light yield, which means how many optical photons are generated for an incoming particle. The yield is also shown in the right side of Figure 3.4, it is particle dependent, because the particles interact in different ways inside the scintillator material, as explained in theory chapter 2. The data is taken from the manufactures-website [13].
Other properties that are also important are the decay time constants,

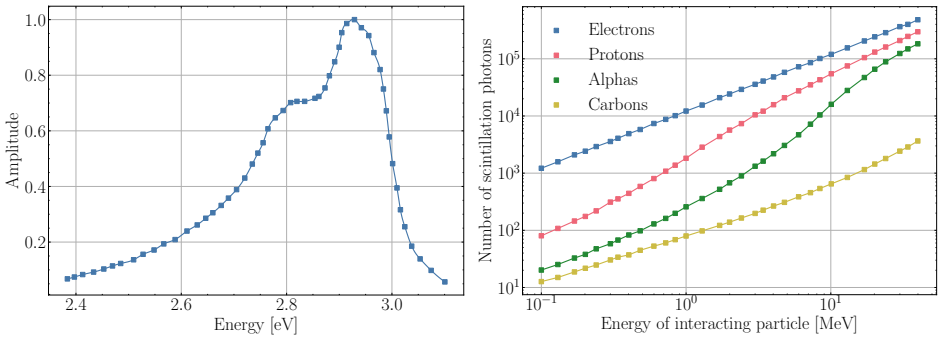

(a) emission spectrum **(b)** light yield

Figure 3.4.: Used properties of EJ301 liquid scintillator, the wavelength of maximum emission is at an energy of 2.92 eV, that equals 425 nm, this corresponds to blue light. The resulting light yields are different due to the different ways in which different particles interact in the material. As can be seen by the right hand side of the figures, neutrons generate less optical photons than gammas because their secondary particles are either protons, alphas or carbons, where gammas only interact with the electrons.

there were introduced in the section 2.2.1. These are also particle-dependent, which is why neutrons and gammas have different pulse shapes by which they can be distinguished. Table 3.1 shows the constants, which were used in the simulation.
The material itself was defined in Geant4 using the values from table 3.2, it is constructed inside the code, with the proportions of helium and carbon atoms and how they occur in the organic structure. These densities are the only information given by the manufacturer, they do not give the exact

Table 3.1.: Time Constants for EJ301 liquid scintillator taken from [14]

Particle	Fast		Medium		Slow	
	t_f [ns]	Impact [%]	t_m [ns]	Impact [%]	t_s [ns]	Impact [%]
Gamma	4.01	89	32	7	160	3
Neutron	5.20	51	32	23	130	17

structure of the organic molecule. The table contains two other important values. The refractive index of the scintillator and the absorption length. This specifies the distance over which the intensity is reduced by a factor of 1/e.

Table 3.2.: General properties of EJ301, the densities define the organic scintillator structure inside Geant4, refractive index and absorption length are important properties for the optical processes of scintillators

property	value
H-Atoms per cm^3	4.82×10^{22}
C-Atoms per cm^3	3.98×10^{22}
Density	$0.874\,g\,cm^{-3}$
Refractive index	1.503
Absorption length	2.5 m

EJ276 - Plastic scintillator In current research, plastic scintillators are becoming increasingly popular, the reason for this is that they are easier to handle. The disadvantage is that their PSD properties are slightly worse to the liquid ones, but their PSD properties have improved in recent years.
A quite common material for PSD is the EJ276 from *Eljen Technology*[15], its used properties can be seen in 3.5, its decay time constants are defined in Table 3.3 and the general properties in table 3.3. In comparison to the EJ301 light yield, it shows that the yield is slightly lower for all the different particles. This means the light output for plastic scintillators is generally lower, so the signal is influenced more by other effects like noise. The result of this is that the pulse shape discrimination capabilities should be worse than for liquid scintillators.

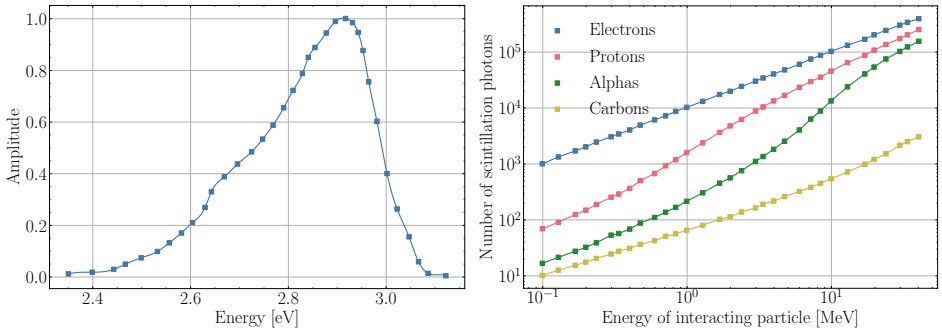

(a) emission spectrum **(b)** light yield

Figure 3.5.: Used properties of EJ276 plastic scintillator, again is the wavelength of maximum emission at 425 nm or 2.92 eV. The light yields are also similarly distributed as in the liquid scintillator, but are generally lower. As a result, fewer optical photons are generated on average in the plastic scintillator

Table 3.3.: Time Constants for EJ276 plastic scintillator taken from [16]

particle	Fast		Medium		Slow	
	t_f [ns]	Impact [%]	t_m [ns]	Impact [%]	t_s [ns]	Impact [%]
Gamma	4.6	74	19	14	130	12
Neutron	5	58	22	18	180	24

Table 3.4.: General properties of the EJ276 and it's material [15]

property	value
H-Atoms per cm^3	4.647×10^{22}
C-Atoms per cm^3	4.944×10^{22}
density	$1.099\,g\,cm^{-3}$
Refractive Index	1.58
Absorption length	1.2 m

3.2.3. Simulated particles and yields

Due to the planned experiment, neutrons and gammas from spontaneous fission of ^{252}Cf are simulated. The data is taken from **A General Description of Fission Observables** (GEF) [17], a simulation program that simulates the process of nuclear fission.
The physics of the prompt particles are simulated with GEF, the results has to be defined within the **PrimaryGeneratorAction** of Geant4. This

simulation uses the General Particle Source (GPS). The energy yields are shown in Figure 3.6, for neutrons it is a continuous function. Gammas have discrete energy values depending on the excitation state of the nucleus involved.
Otherwise, the particles are generated 20 cm in front of the scintillator and directed straight at it.

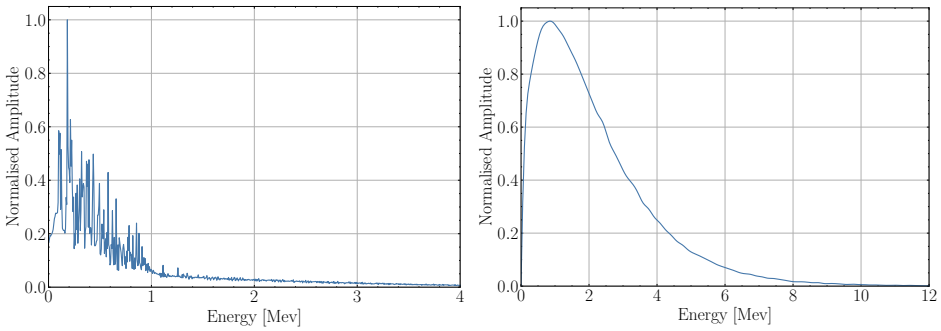

(a) Gammas **(b)** Neutrons

Figure 3.6.: Energy distributions for ^{252}Cf spontaneous fission, generated with GEF [17]. The prompt gammas have individual energies, mostly below 1 MeV, this is the result of the different involved child nuclides and their excitation states. The prompt neutrons have a continuous distribution, with a maximum of around 0.92 MeV and a mean of 2.2 MeV.

3.2.4. Example runs

Just to get an impression of the simulation, an example run is shown in Figure 3.7 for each of the two geometries.

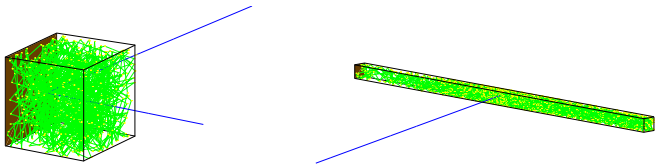

(a) **(b)**

Figure 3.7.: Example runs for both geometry, the incident particle is shown in blue, it is a gamma event. Inside the scintillators, the optical photons are shown in green, these are often reflected on the walls by the aluminium wrapping. They are mainly absorbed at the orange photocathode. For **(a)** the gamma scatters inside the scintillator and gets out with a lower energy. In **(b)** the gamma is completely absorbed.

3.3. Simulation of electronic effects

Geant4 only simulates the optical photons and their interaction inside the scintillator, at the surface of the aluminium wrapping and photocathode. This means that the electronic processes inside the photomultiplier tube (PMT) and the signal's path through an analogue to digital converter (ADC) are not taken into account by Geant4.
Therefore, a separate class was developed for this work within the Geant4 C++ project that takes these processes into account. The basic principle is shown in Figure 3.8. Each of these steps is explained in detail below.
The simulated PMT is the R9800 from *Hamamatsu* [18], and its used properties are listed in Table 3.5.

Table 3.5.: Properties of the PMT R9800 from *Hamamatsu* [18]

property	value
Material of Photocathode	Bialkali
Gain	1.1×10^6
Transit Time Spread (FWHM)	270 ps

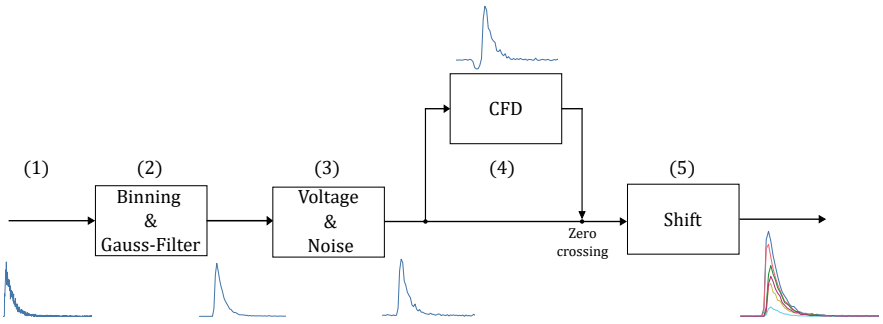

Figure 3.8.: Schematic structure of the processes to simulate the Electronics, the raw signal of the optical photons that hit the photocathode (1) is re-binned and a Gaussian filter is applied (2), to simulate the transit time spread (TTS) inside the PMT, due to the high number of electrons and their varied paths. After that the y-axis is scaled to a voltage, through the gain of the PMT, white noise is applied (3). With a constant fraction discriminator (CFD) (4), the signals are placed at the same starting (5) point by a determined zero-crossing mimicking the behaviour of an ADC.

Quantum Efficiency An important process to include is the quantum efficiency of the photocathode, photoelectrons[2] are released in the photocathode by the optical photons through the photoelectric effect. This effect is influenced by a probability, the quantum efficiency, the quantum efficiency used in the simulation is plotted in Figure 3.9.

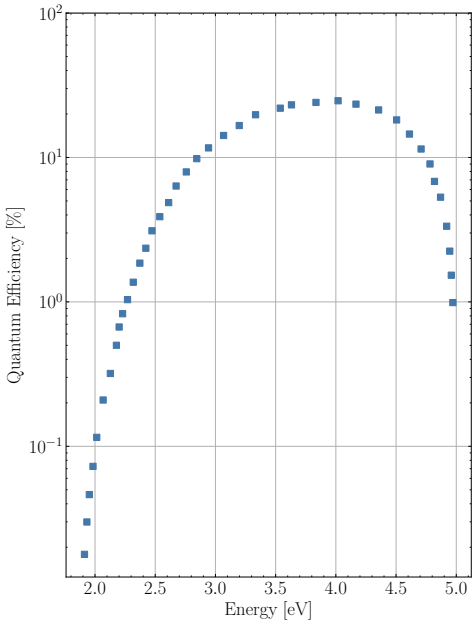

Figure 3.9.: Quantum Efficiency in dependence of energy of the optical photon. The energy range equals wavelengths between 250 nm to 650 nm. For the expected optical photons inside the scintillator with 2.4 eV to 3.1 eV, the quantum efficiency is about 5 to 20%. That means many photons get lost in this process. This data is taken from the data-sheet of the PMT used in the simulation [18].

Binning The signal has to be binned to form a pulse shape. The ADC only measures how many events arrive at a moment in time with a binned resolution. A time resolution or bin width of 1 ns is selected, this is fast but today's analogue to digital converters can achieve such rates. These rates are necessary to be able to record detailed pulse shapes for differentiation between gammas and neutrons.

2A photoelectron is a low energy photon that has energies/wavelengths in the optical spectrum, something in the range from 380 nm to 750 nm

Gaussian filter It is not accurate that the incoming optical photon is directly saved with its time in the signal path, through the process of many electrons that are generated inside the PMT, these electrons have a transit time spread. The distribution corresponds to a Gaussian distribution, with a certain width, explained in the theory chapter 2.2.2.
The Gaussian filter, applies a Gaussian smearing in a certain window on the data, this is needed because originally the Gaussian function ranges to infinity on both sides. The used with of the Gaussian filter is defined by the Transit Time Spread (TTS) of the used PMT, that is given with a FWHM of 270 ps in Table 3.5. The result of the processes until now can be seen in Figure 3.10.

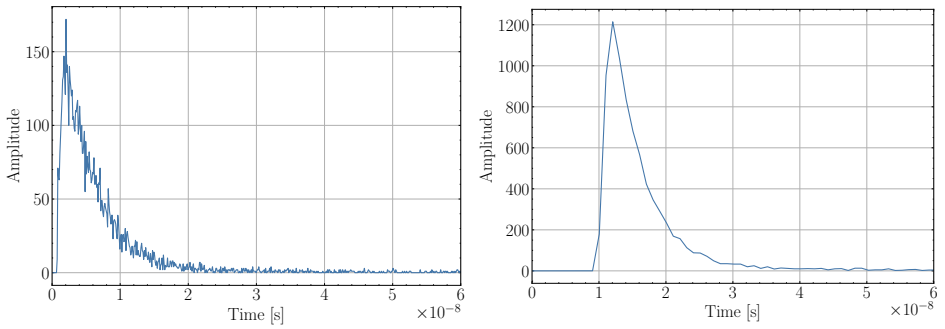

(a) Original Data **(b)** After binning and Gaussian filtering

Figure 3.10.: On the left side, the original data of the individual hit-times of the optical photons on the photocathode can be seen. After the binning with a bin width of 1 ns and applying a Gaussian filter with an FWHM of 270 ps, the shape of the pulse remain the same, but with fewer fluctuations. The pulse was also shifted just to make sure no events on the left side get cut out by the binning. This is shown on the right side.

Convert y-axis to a Voltage For now, the y-axis of the pulses has units of absolute count rate of optical photons, but in the experiment, voltage is measured. This step is necessary to apply noise to the data and simulate a realistic pulse shape.
The absolute count rate per bin n is known, and the average gain of electrons that are generated through the PMT is known, given in Table 3.5. This means that the charge per bin Q can be calculated, since the charge of an electron with the elementary charge e is also known:

$$Q = n \cdot \text{gain} \cdot e \tag{3.1}$$

Where is Q the charge per bin and n the absolute count rate of optical photons. It is known that the current i is given by:

$$i = \frac{\mathrm{d}Q}{\mathrm{d}t} \tag{3.2}$$

That means i is given with the differential charge q for a differential time t. Since Ohm's law is also known and a typical impedance R of $50\,\Omega$ is chosen, the voltage per bin can be calculated:

$$u = \frac{n \cdot \mathrm{gain} \cdot e}{\mathrm{d}t} R \tag{3.3}$$

Where $\mathrm{d}t$ is the bin width.

Electronic Noise Through the previous step, a noise can now be applied to the data. There are various sources of noise in the electrical processing chain, one of the main sources being the ADC. Gaussian noise was simulated with a typical and realistic value of a sigma of10 mV, which is the maximum amplitude of the noise.
The result of this is that the events with lower light output are more affected by the noise, than events with higher light output.

Constant Fraction Discriminator So that the pulses can be compared later, they must be placed on top of each other. A simple threshold discriminator is not useful with organic scintillators as the pulse heights are very different due to the different light outputs. That is why it is difficult to set a threshold without a so-called time walk effect, where the pulses after the discriminator are still shifted depending on their amplitude.
A better option is the constant fraction discriminator (CFD), this device is technically easy to implement. It finds the maximum of a pulse by a simple manipulation of the pulse itself, a graphical differentiation. Figure 3.11 shows the principle of a CFD.

Shift Pulses to Same Trigger The last step of the signal processing is shifting the pulses to the same trigger point. This point was already determined through the CFD, the program shifts this point of each pulse to a value of 10 ns. To avoid accidentally cutting off the signal in the desired range of 150 ns, the in Geant4 saved signals have a longer range. The result of this process and therefore the end of the Monte-Carlo generated data processing path can be seen in Figure 3.12.

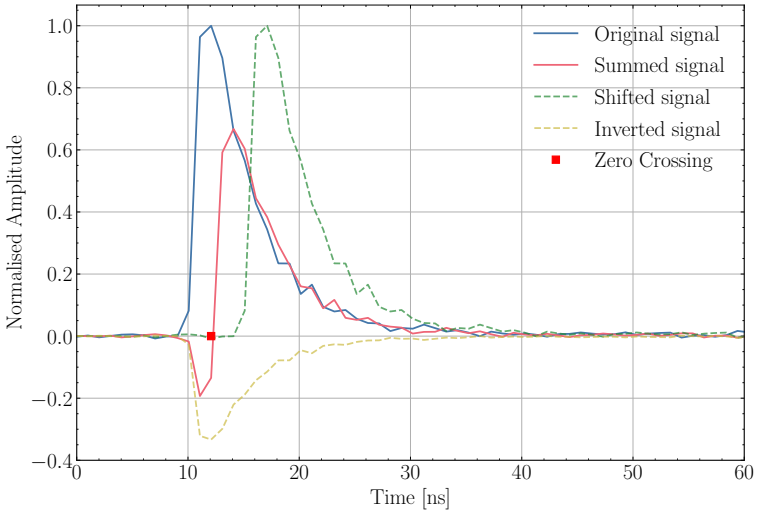

Figure 3.11.: Basic principle of the constant fraction discriminator, the incoming signal (blue) is split into two signals. One is shifted so that the peaks are no longer completely on top of each other (dashed green) and the other one is multiplied by a constant fraction and inverted (dashed yellow). After that, the two pulse signal paths are summed back together (red), the resulting zero crossing point is used as a trigger.

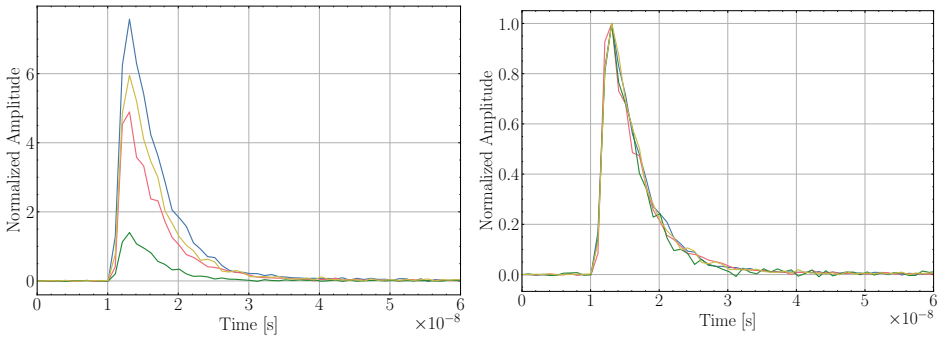

(a) **(b)** Normalized

Figure 3.12.: Some resulting gamma pulses, after shifting to the same trigger point via the CFD. When they are not normalized, the different heights/ light outputs are visible. In the normalized plot, they align perfectly together through the shifting, these normalized pulses are later used for the pulse shape discrimination.

This chapter has shown how the simulation of pulse shapes for neutrons and gammas inside organic scintillators was done using Geant4. The aim was to get as close as possible to experimental pulses, which is why the electrical effects of a PMT or the noise of an ADC were also simulated.
In the next chapter, these pulse shapes are analysed and the DNN is trained with these pulse, to perfrom a pulse shape discrimination between neutron and gammas.

4. Pulse Shape Analysis

The pulse shapes that were created in the last chapter by a Monte-Carlo simulation are now analysed using two different methods. First the old method of pulse shape discrimination, the charge integration method and after that, as the main investigation of this work, the analysis of the pulses with a deep neural network.

4.1. Results from Simulation

The plots in Figure 4.2 show the resulting pulse shapes from the Monte-Carlo simulation of the previous chapter. For the plastic EJ276 and liquid EJ301 scintillator, 1000 pulses were added together for each plot, to see the general trend.
A time series of single pulses can be seen in Figure 4.1, the pulse heights appear randomly. It is important to investigate this to check if the Geant4 random generator has no pattern. In appendix A are shown some random single pulses for neutrons and gammas each. They are normalised, and it can generally be seen that neutron pulses contain more noise, the reason is the lower light output of neutrons in organic scintillators.
To train the deep neural network, a threshold of 100 mV is applied to the data. This means only pulses with a maximum value above this threshold are used for training. This is important because the DNN can only learn well when the data has a clear structure and is not too noisy.

An important step, before any pulse shape discrimination can be done, is the normalization of the data. Each pulse is normalized so that the maximum value of the pule has a value of 1, only so are the pulses and their areas comparable and this is the only way a deep neural network can find patterns.

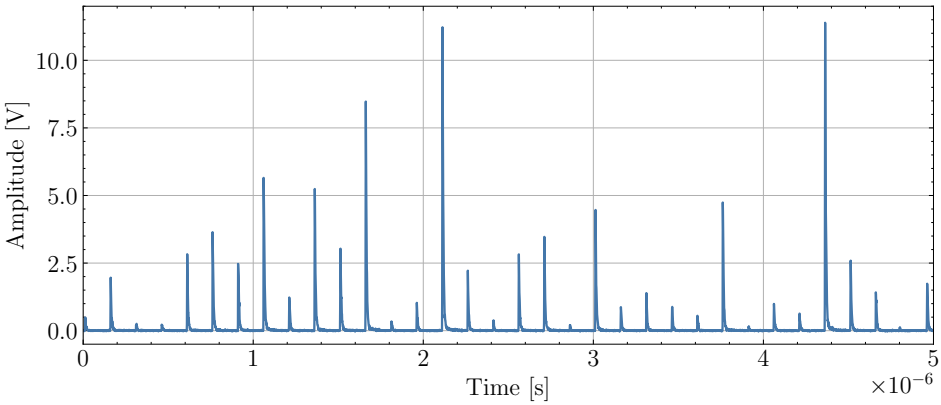

Figure 4.1.: Continuous time series of the simulated pulses, it can be seen that the pulse heights are randomly distributed. It is important to check this so that the random generator of Geant4 does not have a specific pattern.

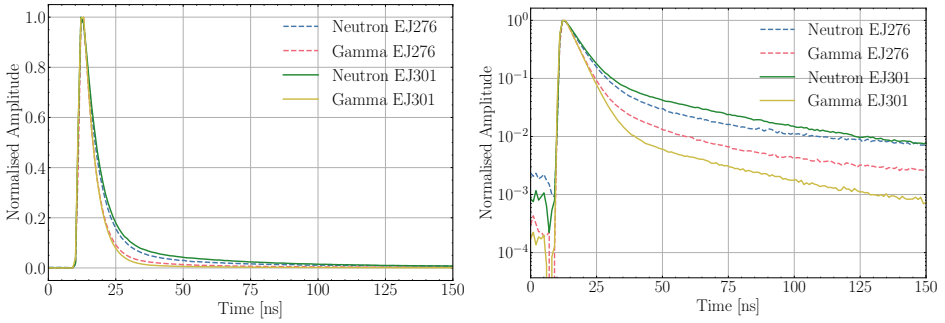

(a) Linear **(b)** Logarithmic

Figure 4.2.: Resulting Pulse Shapes for both simulated scintillators, for every 1000 pulses summed together, in linear and logarithmic scale. The difference between Neutron and Gammas is clearly visible. The logarithmic plot shows that the EJ301 liquid scintillator will have a better PSD performance because the particle pulses have a wider distance in amplitude to each other. The offsets before the rise of the pulses, seen in the logarithmic plot, are caused by the Gaussian filtering, not an experimental effect.

4.2. Charge integration method

The charge integration method is the previously well established method how to distinguish between Neutrons and Gammas.
The principle is rather simple, because the neutrons have in general a longer tail, that means they have a larger area under this tail in comparison to gammas. To quantify this effect, the PSD-value is defined, it is simply the

ratio of the tail-area to the total area:

$$\mathrm{PSD} = \frac{Q_{\mathrm{tail}}}{Q_{\mathrm{total}}} \tag{4.1}$$

The total Area Q_{total} is defined as, the area from the maximum of each pulse to the maximum range of 150 ns. The tail area Q_{tail} starts 8 ns after the maximum and also until the maximum time range. This delay is used because the pulses start to differ from this point.
An important value to compare the PSD capabilities of different scintillators is the FOM:

$$\mathrm{FOM} = \frac{S}{n_{\mathrm{FWHM}} - \gamma_{\mathrm{FWHM}}} \tag{4.2}$$

Where S is the difference between the two peaks of the PSD distribution and n_{FWHM} and γ_{FWHM} are the full width at half maximum for the peaks. The higher this value gets, the better the discrimination is. This is a relative value for comparison only and does not indicate efficiency.

4.2.1. EJ301

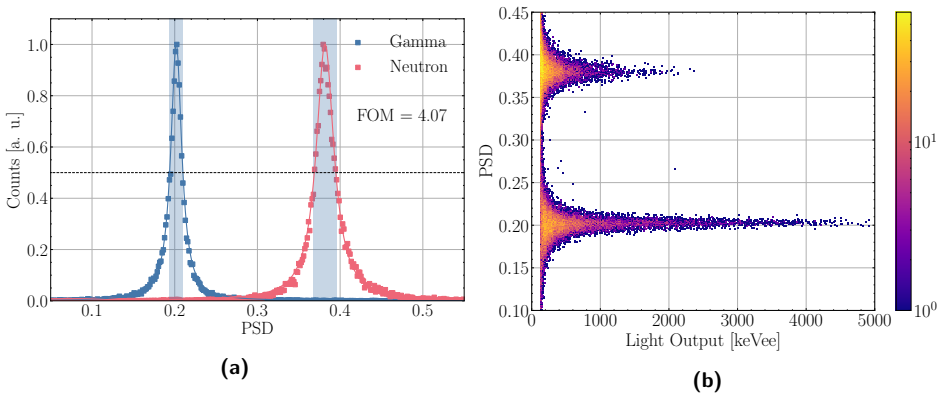

Figure 4.3.: The liquid EJ301 shows extremely good PSD capabilities, as the two peaks for gammas and neutrons are far apart. The PSD-values follow a Lorentz distribution, triggered by low light output events. The 2D-histogram shows also the the dependence on the light output, even with low light outputs the peaks are still easy to distinguish.

The result of the liquid scintillator can be seen in Figure 4.3, it shows excellent PSD capabilities. In the histogram, it can be seen that the PSD values follow a Lorentz distribution, this is a result of the low light output events. They have a lower statistic and are more influenced by noise, which means their fluctuation is greater.

The resulting FOM is 4.07, this is a very high and unrealistic value, [19] shows in an experimental setup a FOM of 2.15. A reason for the high simulated value could be that in real experiments, the light output of scintillators is usually lower than indicated by the manufacturer, and also, the noise of the electrical signal chain can be higher than simulated. As a result, the deviations are greater and the PSD-peaks wider.
A common representation is a 2-dimensional histogram, with the electron-equivalent energy to the PSD-value. To get this equivalent energy, a calibration has to be done. One of the advantages of Geant4 is, that it is possible to know out the energy deposition of the primary particle. On the other side, we know the pulse height in volts V for each event. With this information, a linear regression was performed to get a correlation between the pulse height and the energy equivalent in keV. The regression can be seen in appendix B.1.
The resulting plot shows two peaks, similar to the 1-dimensional PSD-plot, with a separation in the energy direction. It can bee seen, that low light output events are harder to distinguish, but still good for theses type of scintillator.

4.2.2. EJ276

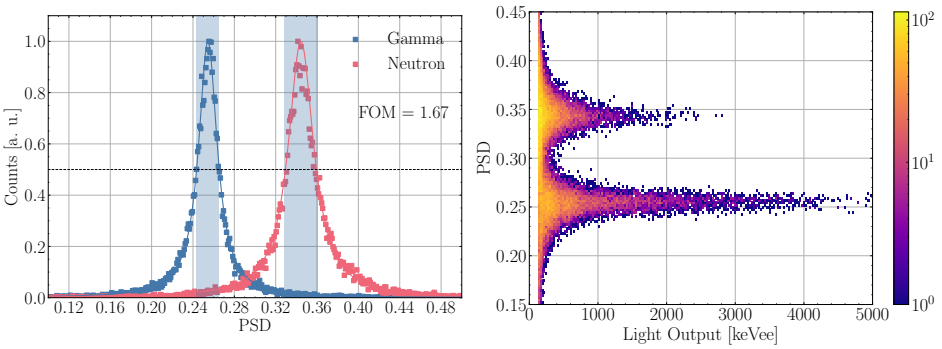

Figure 4.4.: PSD plots for the plastic EJ276 scintillator. The neutron and gamma PSD-values are closer together, the distribution functions a little wider as for the EJ301 scintillator. Therefore the FOM is lower with a value of 1.67. The 2D-histogram in (b) shows that low light output values are not clearly assignable in the region between the peaks.

For the results of the plastic scintillator shown in Figure 4.4, the two PSD peaks are closer together. This was to be expected due to the lower scintillation yields and the time constants that were closer together. This result compares well to experimental results, in general, are plastic scintillators worse than liquid ones. Also, a FOM value of 1.67 is a good and reasonable result in comparison to [19] with a FOM of 1.15, still a bit lower due to the experimental effects but in the same region.

4.3. Deep neural network

For this classification problem, a Deep Neuronal Network is used (DNN), it consists of an input layer and an output layer, between them are multiple hidden layers, the details were explained in section 2.3. The main advantage of the network in comparison to the charge integration is, that the network can learn more information about the shape of the pulse, than only two values with the tail and total area. Therefore it gets as input the whole pulse shape, that means a series of 150 values, each with a time difference of 1 ns.

4.3.1. Structure of DNN

The **keras** [20] software package was used to implement the DNN, it is a **python**-package that uses **TensorFlow** [21], Tensorflow is a open source machine learning library. The network is mainly based on the network from [22]. In more detail a sequential keras-model was used, that defines the used layers of the network in a row. Three hidden layers were used, with a decreasing number of neurons, as shown in the schematics Figure 4.5 of the network. The network is a fully connected neural network, because every neuron of a layer, is connected to every neuron in the next layer.
The network consists of many so-called hyper-parameters, these parameters have to be tuned to get optimized classification results. The optimized and used parameters can be seen in Table 4.1. The dataset used for training was the simulated data with an even split for neutron and gamma pulses, and an equally large split for EJ276 and EJ301 pulses. In the end 40 000 pulses each were used. A train-test-split of 70-30 was used. That means 70 % of the data is used as training samples, the rest later for testing, it should be noted that the data was randomly mixed before this split.
The network was trained for 80 epochs, which was the best value for a good but not yet overfitted DNN. In each of these epochs, the network is learning

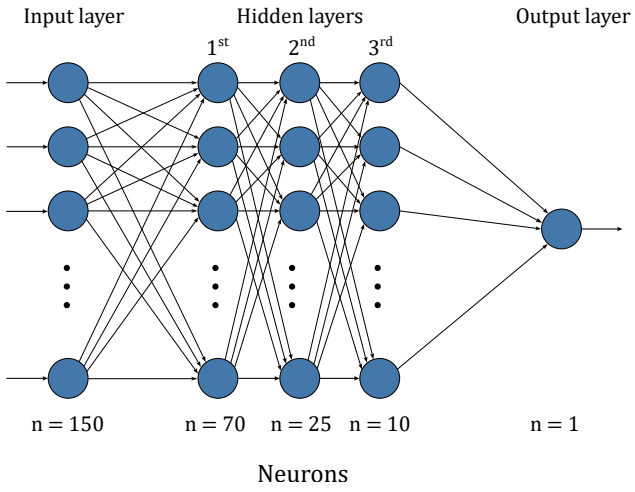

Figure 4.5.: Structure of the used DNN network architecture, it consists of 3 hidden layers, with a decreasing number of neurons. The input layer has 150 neurons and consists of the pulse shape as a vector and the output layer has only one neuron, as this is only a binary classification problem

with the whole training dataset and validating its results with 10 % of the training dataset. It was trained with a learning rate of 0.01 and a batch size of 128, that means after 128 samples, the DNN is changing its weights slightly in the range of the learning rate. With the Adam optimizer, this learning rate is adaptively adjusted.
For the input and hidden layers, a ReLu activation was used, it is a helpful activation function for complex data sets, the function can expressed as $f(x) = \max(0, x)$, a linearly increasing function, starting from 0. For the output layer a sigmoid function decides between two states, one for gammas and the other for neutrons. The loss function compares the predicted values with the validation values, therefore a binary-cross-entropy is used. A function that determines the difference from the probability for the predicted value, from the known validation value.
A problem that often occurs in the training of deep neural networks is overfitting, that means the network is learning specific properties of the training data, but not for the general problem. The data was quite susceptible to overfitting, to counteract this, first of all the neurons in the hidden layers were minimised to optimal values. This way, the network is forced to filter out the important features and does not learn fine details such as

noise of the training data. The second solution was to apply an L2 kernel regularization to the hidden layers with an optimized parameter of 0.001, the exact function of these was explained in 2.3.

The plots in 4.6 showing the training procedure of the network, the loss

Table 4.1.: Hyperparameters of the DNN

Hyperparameters	value
Training samples	112 000
Validation samples	11 200
Testing samples	48 000
Epoch	80
Batch size	128
Learning rate	0.01
Optimizer	Adam
Input Dimension	150
Hidden layers	3
Neurons in first hidden layer	70
Neurons in first second layer	25
Neurons in first third layer	10
Input activation function	Relu
Activation function in hidden layers	Relu
Output activation function	Sigmoid
Loss function	Binary-cross-entropy
Kernel regularizer in hidden layers	L2 with 0.001

is just the negative version of the accuracy, both are improving over time. After training, an accuracy of about 98.8 % on the training data and 98.6 % on the test data is achieved. This is a good result and checked further in the section 4.3.3.

4.3.2. Feature analysis

A DNN is a bit like a black box from the outside, it is unclear which values it has used as a basis for the classification. A software package to obtain information about this process, is **SHAP** (**SH**apley **A**dditive ex**P**lanations) [23]. It analyses the decisions of the network and assigns weights to the input features, these indicate how important this value was for the decision. A comparison of these shap-values with the pulses can be seen in Figure 4.7. It shows that the most significant impact has the time series between 20 ns

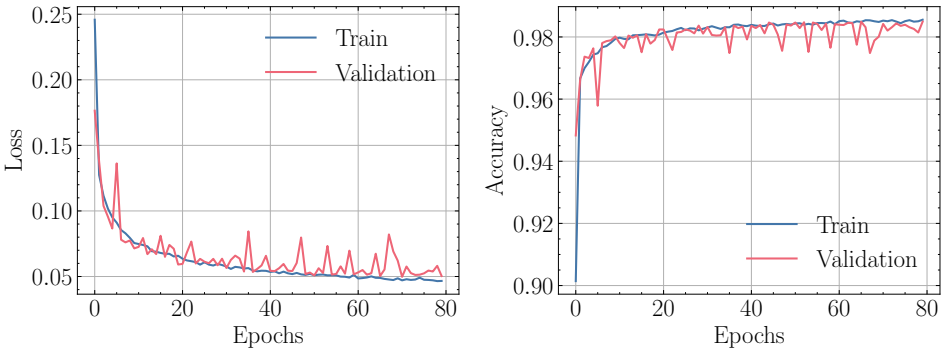

Figure 4.6.: Training procedure of the network, with increasing epochs, the loss decreases and the accuracy increases respectively. The validation data set achieves values similar to those of the training data set, but with higher fluctuations. The training is stopped when the validation is still close to the training data. With higher epoch values, the model would be run into overfitting.

to 40 ns, this is a good result, because in this time range the difference between the gamma and neutron pulses is the largest. Also an important decision was taken at the peak of the pulse, this is not optimal, because there should be no difference, but there is a recognisable difference in the training data, this is probably an error due to the binning in the 1 ns steps.

4.3.3. Testing the DNN

Simulated pulse-shapes As the pulse shape discrimination capabilities for the simulated liquid and plastic scintillators are very different, as seen in section 4.2, these are also tested separately with the network. For testing, 12000 samples per scintillator were used.

An important characteristic of the performance of an DNN is the confusion matrix, these matrices for the both scintillators can be seen in Figure 4.8. As explained in the theory section 2.3, from these matrices characteristic values for the performance can be calculated, these are shown in Table 4.2. Overall, the metrics show that the DNN is performing well on the training data, the liquid scintillator achieves extremely good results with an accuracy of 99.6 %, and the separate values for neutrons and gammas are nearly the same. The plastic scintillator EJ276 is also performing good, but slightly worse than, its gamma precision is98.2 %, a bit better then its neutron precision with 97.6 %. The recall values are roughly reversed. That means in the end that the F1 score, that is the harmonic mean of recall and precision, is nearly the same with around 97.7 %. That is also nearly the

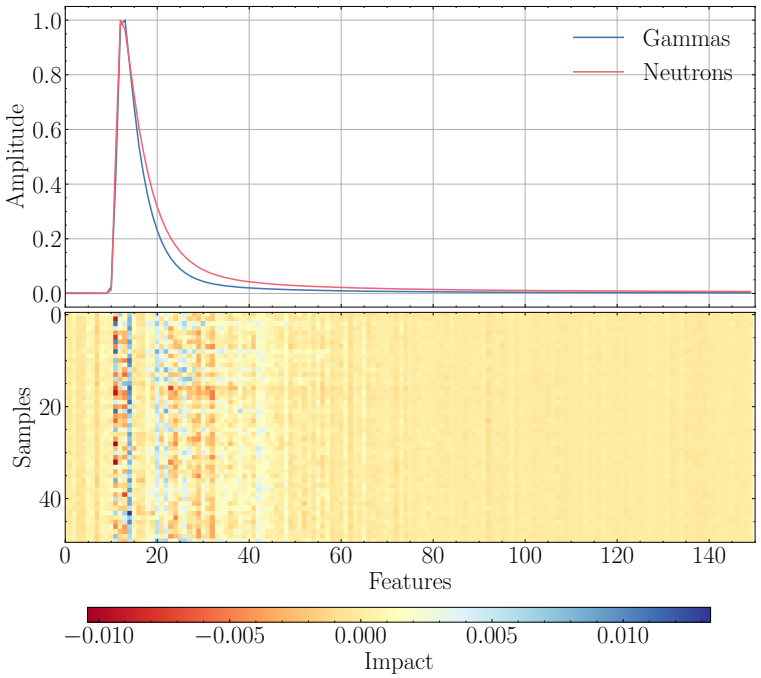

Figure 4.7.: Results for the SHAP-analysis, the heatmap at the bottom shows the impact of the feature on a decision. This is illustrated for various samples, where each sample consists of 100 original pulses to improve the statistics. At the top can be seen the summed training pulses for neutrons and gammas each. A good result is that in the time range of the largest difference between the pulses of neutrons and gammas, the features have a higher impact. Earlier features for the shorter gamma pulses and later ones for the longer neutron pulses. A small error in the training data set is the small difference in the pulses at the peak at around 11 ns, this is due to the division into 1 ns steps. This peak difference also has an influence on the model.

accuracy of the test data for the plastic scintillator.
These results were to be expected, as the liquid scintillator also had better discrimination properties than the plastic scintillator with the charge integration method in 4.2. The charge integration and DNN methods are compared with each other in the discussion in chapter 5.

Experimental data In order to test the network not only with simulated data, it is now tested with actual measurement data. This data is from the experiment in [24]. The data consists of 5000 neutron pulses and 15000 gamma pulses.
The first step in processing the data was to invert them and subtract the

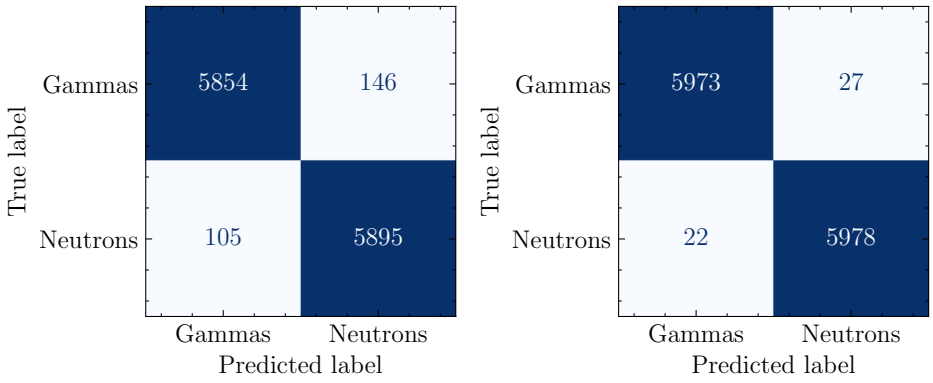

(a) EJ276 **(b)** EJ301

Figure 4.8.: Confusion matrices for plastic and liquid scintillator. As the test data set has the same size of 12000 samples each, it is immediately clear that the liquid scintillator EJ301 performs slightly better than the plastic scintillator

Table 4.2.: Performance of the test dataset for both scintillators

	EJ276		EJ301	
	Neutron	Gamma	Neutron	Gamma
Precision	0.9758	0.9824	0.9955	0.9963
Recall	0.9825	0.9757	0.9963	0.9955
F1-score	0.9792	0.9790	0.9959	0.9959
Accuracy	0.9791		0.9959	

baseline of 892 units. The plot on the left side of Figure4.9, shows the structure of the pulses after these steps. It can be seen that the data is much wider than the simulated data, the rise time is clearly longer and also the decay times are longer. A reason for this could be a strong smoothing of the data. An oscillation can also be observed in the data, which may be due to errors in the measurement setup.

In order for these pulses to be processed by the network, the pulses must be similar to the simulated training data. As a solution, the data was compressed, and 2 values were combined into one. The resulting pulses can be seen on the right side of Figure 4.9. Now they fit better with the simulation data, but they still differ, for example in the oscillation.

As figure 4.10 and Table 4.3 show, the DNN also performs well with the

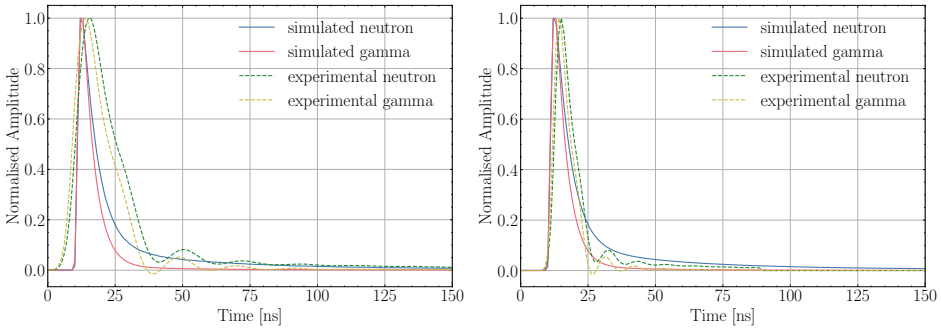

(a) Original **(b)** After processing

Figure 4.9.: Experimental data in comparison to simulated data, both for the liquid scintillator EJ301/BC501. The original experimental data were much wider than the simulated data, so they were compressed to the half and the pulses were shifted so that all maxima were approximately on the same time level

measurement data. With an accuracy of 98.5 %, it performs better than the plastic scintillator data. Its performance for the classification of neutrons is with a precision of 99.8 % extreme good, but it misclassifies some gammas as neutrons, so the gamma precision is only 98 %.

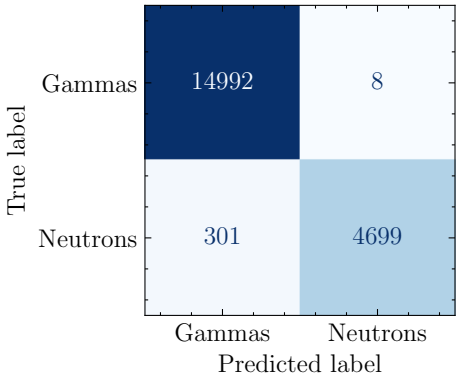

Figure 4.10.: The confusion matrix for the measured data shows, that the DNN is also preforming good with this data.

	Neutron	Gamma
precision	0.9983	0.9803
recall	0.9398	0.9995
F1-score	0.9682	0.9898
accuracy	0.9846	

Table 4.3.: Performance of the experimental test dataset

5. Results and discussion

So far, two methods for pulse shape discrimination have been presented: the charge integration method and the method of classification using a deep neural network. In the following chapter, these methods are compared with each other. A good method for this is the ROC plot, which is well-suited for comparing different classifiers and was introduced in section 2.3.3.

5.1. Comparison of ROC-curves

A good tool to compare the performance of classification problems, is the receiver operating characteristic (ROC) curve, these curves were explained in detail in theory section 2.3. The Figure5.2 shows the ROC curves of the 3 test data sets, this plot shows that the simulated liquid scintillator EJ301 delivers almost perfect values. The measured liquid scintillator is a bit worse, but still better then the simulated plastic scintillator EJ276. A comparable value gives the AUC, that is also shown in the Figure 5.2.

This chapter has shown both methods and their results for the pulse shape discrimination between gammas and neutrons. In the next chapter, these methods will be compared to show that a deep neural network has advantages over the old charge integration method.

5.2. Comparison between CI and DNN methods

5.2.1. plastic scintillator- EJ276

Since plastic scintillators will most likely be used in the upcoming experiment, the PSD methods for these scintillators will now be compared. Section 4.2.2 has shown that, the PSD for high light outputs of the EJ276 scintillator, are nearly perfect for the charge integration method. The problem appears at low light output values, some values can no longer be clearly assigned there. The hope would be that the DNN is better at assigning these low light output values.

This is compared in Figure 5.2, the ROC-curves for different thresholds are shown. The highest threshold is 500 mV, it is chosen as a check for high

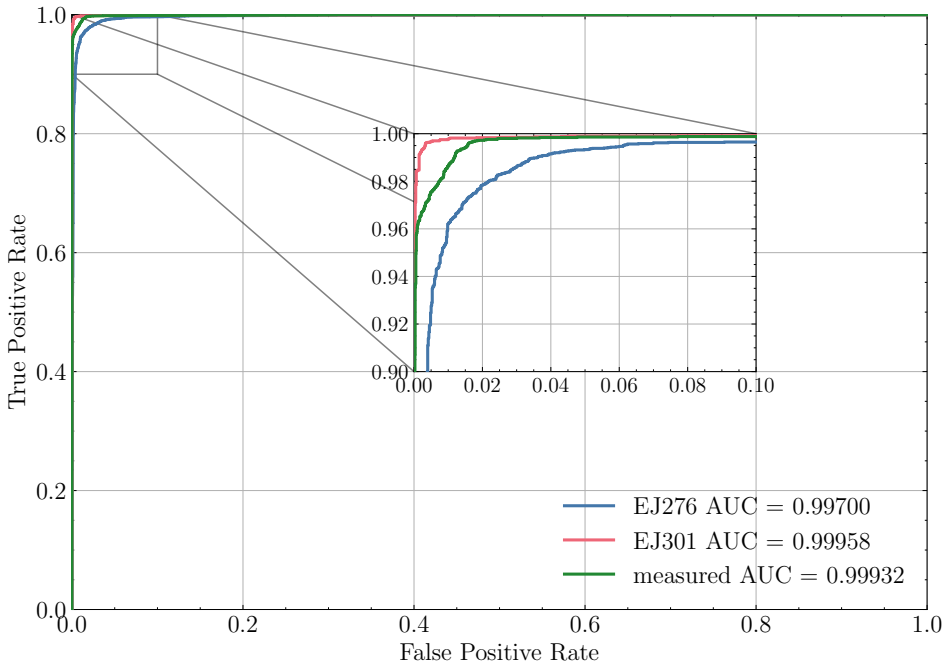

Figure 5.1.: This comparison shows the ROC curves of the test data for the simulated liquid EJ301 and plastic EJ276 scintillator, and also the curve for the measurement data. In order to see the difference better, a zoomed plot is inserted in the upper left corner. The AUC value for all three curves is also shown.

light outputs. It can be seen that for this threshold both methods are not different. The training data of the network has values above 100 mV, already these curves show that the DNN classifies better than the CI method. For even lower light output with 60 mV or 40 mV it is the same.
It should be mentioned that a noise level of 10 mV was selected for the simulation, that means such low light output pulses are extremely noisy, for even lower threshold values the data consists almost exclusively of noise. It should be emphasized that the DNN is better at distinguishing the low noise data between photons and neutrons. Especially if the light output should be even lower in an experimental setup, it is better to use a DNN for pulse shape discrimination.

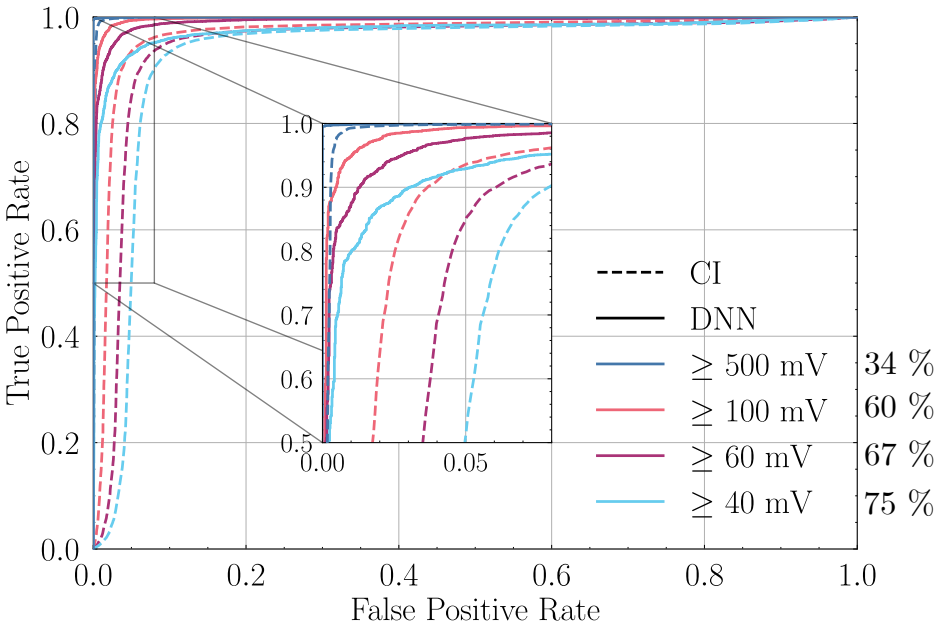

Figure 5.2.: Comparison of ROC-curves for different threshold values. The dashed line shows the CI-method and the continuous lines the DNN results. Basically, the CI curves are worse than the DNN curves, and the curves generally get worse with lower threshold values. It looks like the DNN classifies better between Neutron and Gammas, than the old charge integration method. The percent values show the share of the total data, that means the lower the threshold, the more of the total data collected can be used for data analysis.

5.2.2. Experimental data

The section 4.3.3 has shown, that the trained DNN performed well on the experimental data. A correct conclusion can only be drawn if there is also a comparison of these results with the CI-method. Figure 5.3 shows on the left side the results of the charge integration method, neutrons and gammas can be distinguished mainly well, but still have a large overlapping range, therefore the FOM of 0.59 is quite low compared to the simulated FOM values.
On the right side of 5.3 the ROC-curves are compared to each other. The DNN curve is nearly perfect, as already shown in Section 5.1. The charge integration ROC-curve is clearly worse, this is also shown in the AUC value of 0.957 in comparsion to a AUC of 0.999.

This result proves once again that the deep neural network is better at

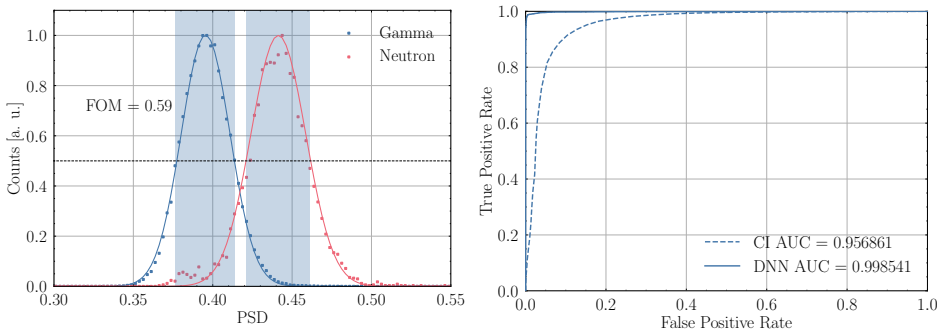

(a) (b)

Figure 5.3.: Figure **(a)** shows the PSD histograms for the measured data, since the distributions are Gaussian distributed, the low light output values are not included in this dataset. For the gammas there were more datasets, so the distribution is cleaner. The neutrons have stronger deviations, as there were only 5000 neutron pulses in the data set. Due to the width of the peaks, the FOM is quite low with 0.59. In **(b)**,the ROC-curves can be seen in comparison between the CI and DNN-method, the DNN-method performs clearly better.

distinguishing the neutron and gamma pulses. Presumably because it makes its decision at points than two integrals. It is general enough to distinguish experimental pulse shapes with artifacts.

5.3. Investigation of different Slab lengths

All previous investigations and the training of the DNN were done for the cube geometry of the Geant4 scintillators, introduced in section 3.2.1. But in the future experiment a more slab shaped geometry will be used, because of this it is important to check if the slab geometry has big changes of the PSD investigation.
The simulated slab was in z-direction 150 cm long and had a base of 5 cm $\times$ 5 cm, the material was the EJ276, as the experiment will use a plastic scintillator. It can be assumed that the pulses change slightly because the optical photons travel different paths in the scintillator or are reflected differently. An overview is shown in figure 5.4, different starting positions in the z-direction were simulated, the PMT was only on one side of the slab. The result is, than the pulses indeed change a bit, the further away the PMT is, the longer the pulses tend to be, because the distance travelled by the optical photons in the scintillator gets longer. But the difference between neutrons and gamma pulses remains the same, therefore a PSD is

still possible.

To check the assumption that the PSD is still possible, the slab pulses were

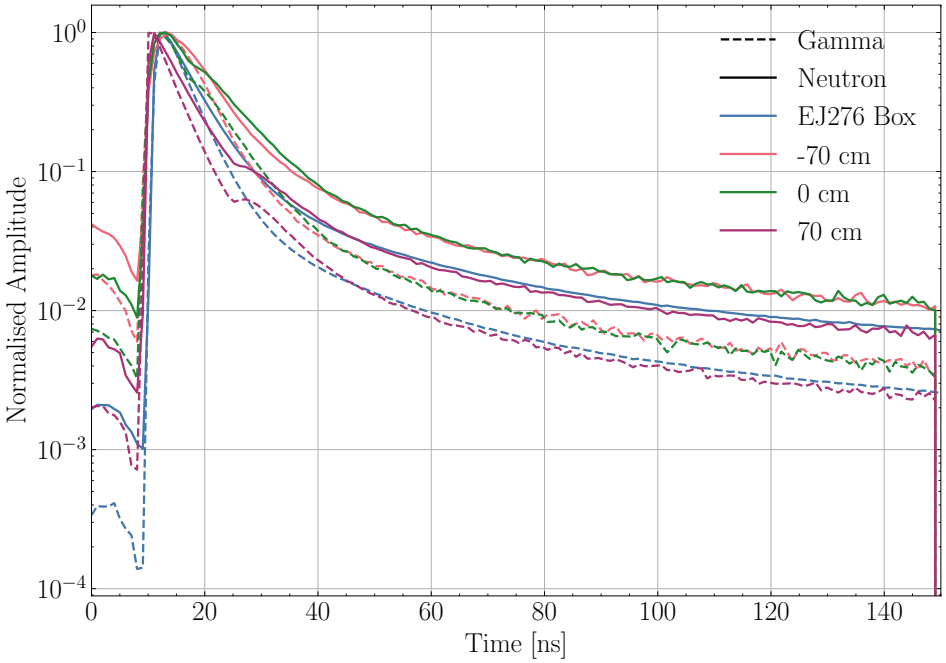

Figure 5.4.: Shown are pulse shapes for different starting positions in z-direction for the slab geometry and for comparison also the pulse shapes of the box geometry. The plot is logarithmic so that the differences can be seen better, in addition, neutrons and gamma pulses are shown separately. The pulses for 70 cm are very similar to the box geometry, but with a bounce at the beginning, probably caused by reflection effects. This was to be assumed as the PMT is placed at 75 cm. The pulses that were recorded for more distant starting positions are generally longer. However, it is important that the difference between neutron and gamma pulses is preserved. This means that a good pulse shape discrimination should still be possible.

used as test data for the trained DNN. The resulting gamma and neutron precisions are shown in Table 5.1. The precision is between 75 % to 98 %, as a general trend, the gamma pulses have higher precision than neutron pulses since the neutrons, as already mentioned, have a lower light output. The second observation is that the precision decreases with increasing distance to the PMT. This can be explained by the fact that the pulses are getting longer, as can be seen in Figure 5.4, and therefore the network is worse in assigning the pulses correctly, as it has never seen such long pulses before.

The last step is to look at the overall efficiency. Therefore 1×10^5 events for various starting positions in z-directions are simulated. In Figure 5.5

Table 5.1.: Precision's of the trained DNN for different starting positions inside slab geometry

z-Position [cm]	Neutron	Gamma
70	0.909	0.971
50	0.933	0.834
30	0.832	0.954
10	0.890	0.914
0	0.821	0.945
-10	0.747	0.962
-30	0.811	0.908
-50	0.866	0.887
-70	0.887	0.870

these efficiencies are shown. On the left side for the already discussed setup, with one PMT located at $z = 75\,\text{cm}$, and and the rigth side a setup with 2 two PMT's on both sides.
Many effects are included in these total efficiencies, at first the neutron and gammas energy distributions of ^{252}Cf, then the interaction of these primary particles with the scintillator material itself. Also, to this the light production and transportation, the processing of the PMT with quantum efficiency is added. The last component is the precision of the DNN shown in Table 5.1 is added.
It is clear to see that neutrons always have a higher efficiency than gammas, this is due to the material, as it is an organic scintillator, it is more sensitive to neutrons. For both setups, the efficiencies are fluctuating, the process behind this is very complex. Because reflections always change the pulse slightly. This results in different performances of the DNN and also different light propagation inside the scintillator itself.
For the one PMT-setup the efficiencies still decreases with increasing distance to this PMT. On the one hand because the precision of the network decreases, on the other hand because fewer optical photons reach the PMT due to the longer distance to travel inside the scintillator. For the PMT on both sides, the efficiencies are symmetrical, with a minimum in the middle area because there is the distance to the PMT's the furthest. But overall the efficiencies are more constant, which is a good result for the future experiment.

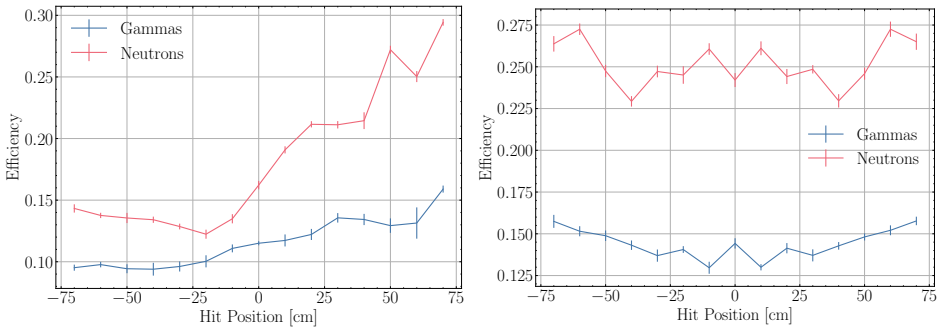

(a) PMT only on right side

(b) PMT on both sides

Figure 5.5.: Overall Efficiency For both PMT setups, neutrons generally have higher efficiencies than gammas. This is mainly due to the higher sensitivity of organic scintillators to neutrons. In general, however, the resulting efficiencies are realistic.

6. Conclusion and outlook

In summary, the method of pulse shape discrimination between neutrons and gammas was investigated in this work. The unique aspect of this work was to simulate pulse shapes using Geant4 and train a deep neural network with them. This DNN was able to classify experimental pulses, even if it did not learn with them. This is an improvement to the previous method, in which experimental pulses are required for training. It is more complex to generate experimental data, but simulation data can easily be generated. In this work, the experimental data had to be edited in order to be classified, since the exact specifications of the set-up, which are required in the simulation, were not known at the beginning of this work. In a further development of the experiment, a few pulse shapes would be recorded in a simple experimental setup, from these, the time constants would be determined in order to perform the Geant4 simulation and train the deep neural network again. Then it can be expected that this new DNN can be used for the entire pulse shape discrimination of the whole experiment. However, it has been shown, that with accurate training of the DNN, it is still able to perform well independent of changes in the properties of the pulse shapes. Chapter 5.2 showed that a DNN classifies better than the previous charge integration method, especially for low light outputs, this is an advantage because more data from the experiment can be processed.
In chapter 5.3, it was shown that a changed geometry, for example a slab geometry as planned for the experiment, has no great influence on the pulse shape discrimination capabilities. Especially when two photomultiplier tubes are used.
In a further development, the deep neural network could also be replaced by a convolutional neural network (CNN), such a network offers even more stable and better results [25].

List of Figures

2.1. Energy Levels for an organic structure 17
2.2. Schematics of aPMT 18
2.3. Transit time spread inside a PMT 18
2.4. Confusion matrix 20
2.5. Basic principle of a ROC-curve 21

3.1. Reflectance of aluminium 23
3.2. Box Geometry 24
3.3. Slab Geometry 24
3.4. Properties of EJ301 25
3.5. Properties of EJ276 27
3.6. n/γ-energy distributions 28
3.7. Example runs 28
3.8. Electronic Signal Chain 29
3.9. Quantum efficiency of photocathode 30
3.10. Data after Gaussian filtering 31
3.11. Basic principle of the constant fraction discriminator 33
3.12. Shifted Pulses 33

4.1. Time Series of simulated Pulses 35
4.2. Summed pulse shapes 35
4.3. Charge integration EJ301 36
4.4. Charge integration EJ276 37
4.5. Deep neural network structure 39
4.6. Training procedure 41
4.7. SHAP-analysis 42
4.8. Confusion matrices EJ301 and EJ276 43
4.9. Experimental pulse shapes 44
4.10. The confusion matrix for the measured data shows, that the DNN is also preforming good with this data. 45

5.1. Comparison of ROC-curves 47
5.2. Compare ROC curves for different thresholds 48

5.3. Comparison of methods for experimental data 49
5.4. Pulse Shapes for different slab lengths 50
5.5. Overall Efficiency for both PMT setups 52

A.1. Some random simulated pulses of the gammas 60
A.2. Some random simulated pulses of the neutrons 61

B.1. Calibration of EJ301 scintillator 62
B.2. Calibration of EJ276 scintillator 63

List of Tables

3.1. Time Constants for EJ301 liquid scintillator taken from [14] 26
3.2. General properties of the EJ301 26
3.3. Time Constants for EJ276 plastic scintillator taken from [16] 27
3.4. General properties of the EJ276 and it's material [15] . . . 27
3.5. Properties of the PMT R9800 from *Hamamatsu* [18] 29

4.1. Hyperparameters of the DNN 40
4.2. Performance of the test dataset for both scintillators 43
4.3. Performance of the experimental test dataset 45

5.1. Precision's of the trained DNN for different starting positions inside slab geometry 51

Bibliography

[1] O. Hahn and F. Strassmann. "Über den Nachweis und das Verhalten der bei der Bestrahlung des Urans mittels Neutronen entstehenden Erdalkalimetalle". In: *Naturwissenschaften* 27.1 (Jan. 1939), pp. 11–15. DOI: 10.1007/BF01488241.

[2] G. Martínez-Pinedo et al. "The role of fission in the r-process". In: *Progress in Particle and Nuclear Physics* 59.1 (2007). International Workshop on Nuclear Physics 28th Course, pp. 199–205. ISSN: 0146-6410. DOI: https://doi.org/10.1016/j.ppnp.2007.01.018. URL: https://www.sciencedirect.com/science/article/pii/S0146641007000099.

[3] Nicolas Schunck and David Regnier. "Theory of nuclear fission". In: *Progress in Particle and Nuclear Physics* 125 (2022), p. 103963. ISSN: 0146-6410. DOI: https://doi.org/10.1016/j.ppnp.2022.103963. URL: https://www.sciencedirect.com/science/article/pii/S0146641022000242.

[4] A N Andreyev, K Nishio, and K-H Schmidt. "Nuclear fission: a review of experimental advances and phenomenology". In: *Reports on Progress in Physics* 81.1 (Nov. 2017), p. 016301. DOI: 10.1088/1361-6633/aa82eb. URL: https://dx.doi.org/10.1088/1361-6633/aa82eb.

[5] Glen Knoll. *Radiation Detection and Measurement (4th ed.)* Hoboken, NJ: John Wiley, 2010. ISBN: 978-0-470-13148-0.

[6] W.R. Leo. *Techniques for Nuclear and Particle Physics Experiments: A How-to Approach*. Springer, 1994. ISBN: 9780387173863.

[7] John B. Birks. *The Theory and practice of scintillation counting*. International Series of Monographs in Electronics and Instrumentation. Pergamon, 1964.

[8] Michael W. J. Hubbard. "Light transport modelling of pulse shape discrimination within plastic scintillators." eng. PhD thesis. University of Surrey, 2020, p. 226. DOI: 10.15126/thesis.00857773.

[9] Aurélien Géron. *Hands-on Machine Learning with Scikit-Learn, Keras, and TensorFlow*. 11 New Fetter lane, London EC4P 4EE: Taylor Francis, 2003. ISBN: 0-203-34540-1.

[10] S. Agostinelli et al. "Geant4—a simulation toolkit". In: *Nuclear Instruments and Methods in Physics Research Section A: Accelerators, Spectrometers, Detectors and Associated Equipment* 506.3 (2003), pp. 250–303. ISSN: 0168-9002. DOI: https://doi.org/10.1016/S0168-9002(03)01368-8. URL: https://www.sciencedirect.com/science/article/pii/S0168900203013688.

[11] S. Agostinelli et al. *LXe Example*. https://gitlab.cern.ch/geant4/geant4/tree/master/examples/extended/optical/LXe. Accessed: 2024-09-01. 2024.

[12] Michael Bass et al. "Handbook of Optics Volume II Devices, Measurements, and Properties 2nd edition". In: McGraw-Hill, Inc., 1995. Chap. 25.15.

[13] Eljen Technology. *NEUTRON/GAMMA PSD, EJ-301, EJ-309*. https://eljentechnology.com/products/liquid-scintillators/ej-301-ej-309. Accessed: 2024-07-29.

[14] T. Szczśniak et al. "Light Pulse Shapes in Liquid Scintillators Originating From Gamma-Rays and Neutrons". In: *Nuclear Science, IEEE Transactions on* 57 (Jan. 2011), pp. 3846–3852. DOI: 10.1109/TNS.2010.2068311.

[15] Eljen Technology. *PULSE SHAPE DISCRIMINATION, EJ-276D EJ-276G*. https://eljentechnology.com/products/plastic-scintillators/ej-276. Accessed: 2024-07-30.

[16] J Iwanowska-Hanke et al. "Comparative study of large samples (2" × 2") plastic scintillators and EJ309 liquid with pulse shape discrimination (PSD) capabilities". In: *Journal of Instrumentation* 9.06 (June 2014), P06014. DOI: 10.1088/1748-0221/9/06/P06014. URL: https://dx.doi.org/10.1088/1748-0221/9/06/P06014.

[17] K.-H. Schmidt et al. "General Description of Fission Observables: GEF Model Code". In: *Nuclear Data Sheets* 131 (2016). Special Issue on Nuclear Reaction Data, pp. 107–221. ISSN: 0090-3752. DOI: https://doi.org/10.1016/j.nds.2015.12.009. URL: https://www.sciencedirect.com/science/article/pii/S0090375215000745.

[18] Hamamatsu. *Photomultiplier tube - R9800*. https://www.hamamatsu.com/jp/en/product/optical-sensors/pmt/pmt_tube-alone/head-on-type/R9800.html. Accessed: 2024-07-30.

[19] Fengzhao Shen et al. "PSD performance of EJ-276 and EJ-301 scintillator readout with SiPM array". In: *Nuclear Instruments and Methods in Physics Research Section A: Accelerators, Spectrometers, Detectors and Associated Equipment* 1039 (2022), p. 167148. ISSN: 0168-9002. DOI: https://doi.org/10.1016/j.nima.2022.167148. URL: https://www.sciencedirect.com/science/article/pii/S0168900222005319.

[20] François Chollet et al. *Keras*. https://keras.io. Accessed: 2024-08-7. 2024.

[21] Martín Abadi et al. *TensorFlow: Large-Scale Machine Learning on Heterogeneous Systems*. Software available from tensorflow.org. 2015. URL: https://www.tensorflow.org/.

[22] Annesha Karmakar et al. "Deep neural network-based pulse shape discrimination of neutrons and -rays in organic scintillation detectors". In: *Pramana* 97 (Sept. 2023). DOI: 10.1007/s12043-023-02641-x.

[23] Scott M Lundberg and Su-In Lee. "A Unified Approach to Interpreting Model Predictions". In: *Advances in Neural Information Processing Systems 30*. Ed. by I. Guyon et al. Curran Associates, Inc., 2017, pp. 4765–4774. URL: http://papers.nips.cc/paper/7062-a-unified-approach-to-interpreting-model-predictions.pdf.

[24] Annesha Karmakar et al. *Development of Indigenous Pulse-Shape Discrimination Algorithm for Organic Scintillation detectors*. 2023. arXiv: 2307.10884 [physics.ins-det]. URL: https://arxiv.org/abs/2307.10884.

[25] J Griffiths et al. "Pulse shape discrimination and exploration of scintillation signals using convolutional neural networks". In: *Machine Learning: Science and Technology* 1.4 (Oct. 2020), p. 045022. DOI: 10.1088/2632-2153/abb781. URL: https://dx.doi.org/10.1088/2632-2153/abb781.

A. Single Pulses

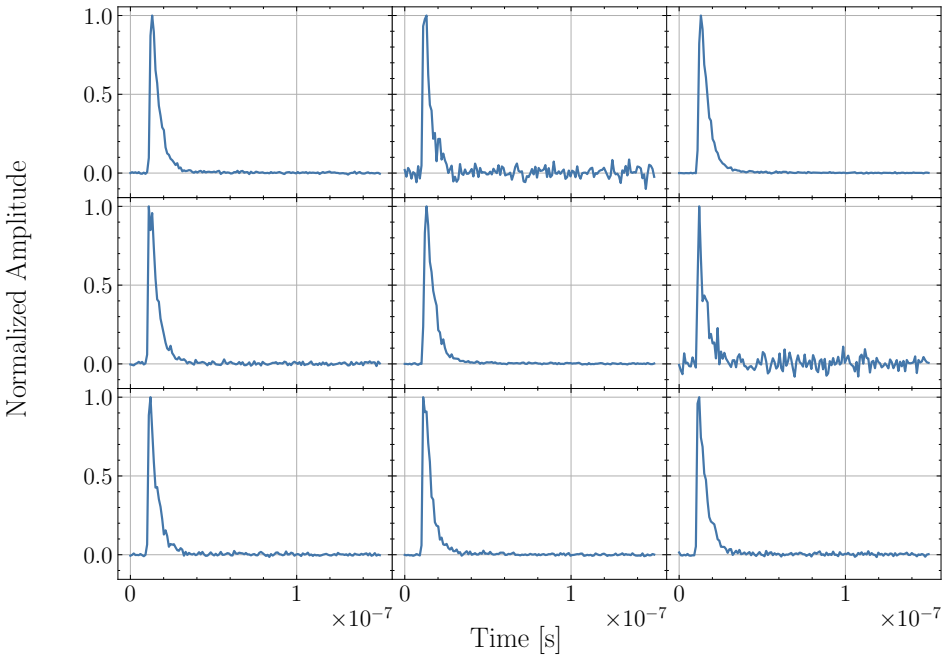

Figure A.1.: Some random simulated pulses of the gammas

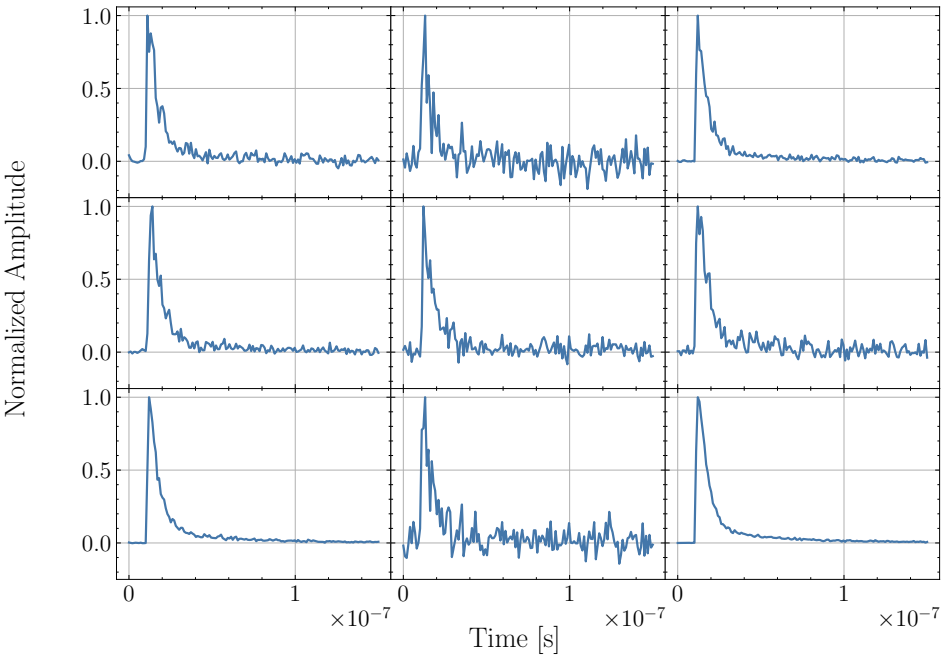

Figure A.2.: Some random simulated pulses of the neutrons

B. Calibration

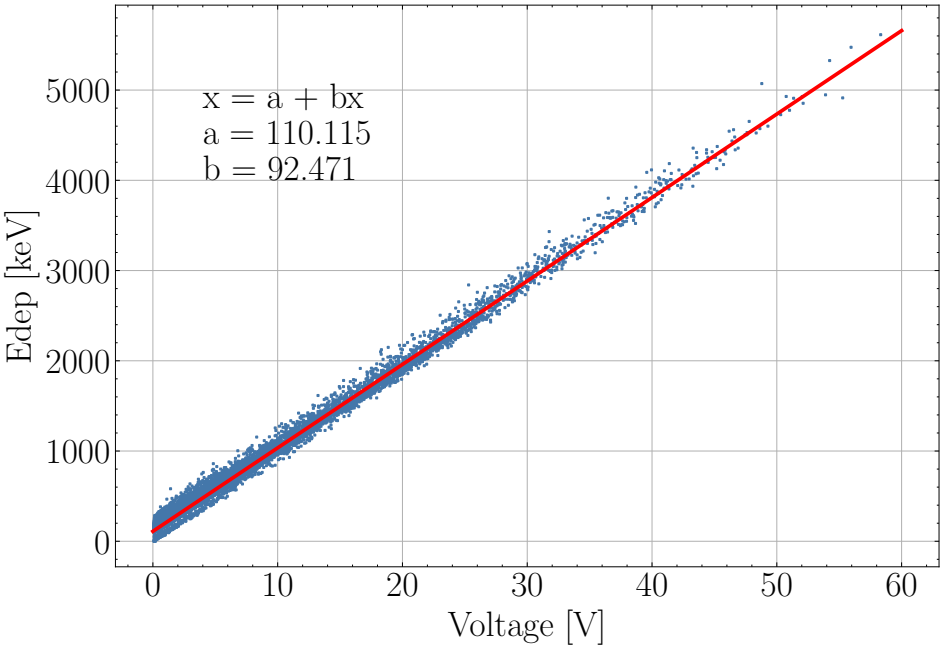

Figure B.1.: Calibration of EJ301 scintillator

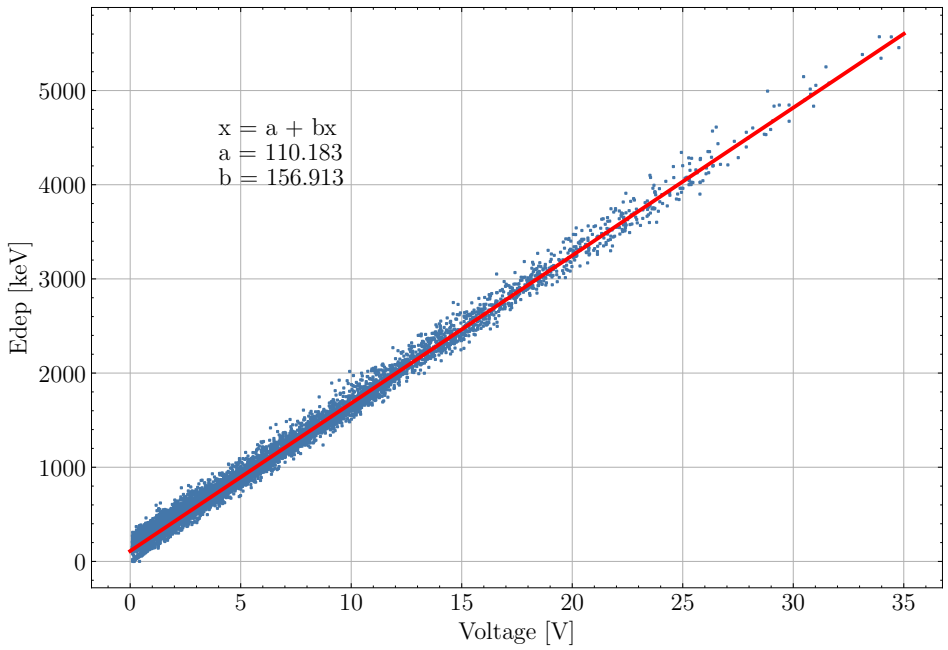

Figure B.2.: Calibration of EJ276 scintillator

Selbstständigkeitserklärung

Hiermit versichere ich, die vorgelegte Thesis selbstständig und ohne unerlaubte fremde Hilfe und nur mit den Hilfen angefertigt zu haben, die ich in der Thesis angegeben habe. Alle Textstellen, die wörtlich oder sinngemäß aus veröffentlichten Schriften entnommen sind, und alle Angaben die auf mündlichen Auskünften beruhen, sind als solche kenntlich gemacht. Bei den von mir durchgeführten und in der Thesis erwähnten Untersuchungen habe ich die Grundsätze guter wissenschaftlicher Praxis, wie sie in der, Satzung der Justus- Liebig-Universität zur Sicherung guter wissenschaftlicher Praxis, niedergelegt sind, eingehalten. Entsprechend § 22 Abs. 2 der Allgemeinen Bestimmungen für modularisierte Studiengänge dulde ich eine Überprüfung der Thesis mittels Anti-Plagiatssoftware.

Frederik Uhlemann
Gießen, 6. September 2024